Coherent structures in wave boundary layers. Part 1. Oscillatory motion

STEFAN CARSTENSEN†, B. MUTLU SUMER‡
AND JØRGEN FREDSØE

Technical University of Denmark, DTU Mekanik, Section of Coastal, Maritime and Structural
Engineering, Building 403, 2800 Kgs. Lyngby, Denmark

This work concerns oscillatory boundary layers over smooth beds. It comprises combined visual and quantitative techniques including bed shear stress measurements. The experiments were carried out in an oscillating water tunnel. The experiments reveal two significant coherent flow structures: (i) Vortex tubes, essentially two-dimensional vortices close to the bed extending across the width of the boundary-layer flow, caused by an inflectional-point shear layer instability. The imprint of these vortices in the bed shear stress is a series of small, insignificant kinks and dips. (ii) Turbulent spots, isolated arrowhead-shaped areas close to the bed in an otherwise laminar boundary layer where the flow 'bursts' with violent oscillations. The emergence of the turbulent spots marks the onset of turbulence. Turbulent spots cause single or multiple violent spikes in the bed shear stress signal, which has profound implications for sediment transport (in both the laboratory and the field). The experiments also show that similar coherent flow structures exist in the case of combined oscillatory flow and current.

1. Introduction

In shallow waters, the orbital motion of water particles under a progressive wave degenerates into a bottom-parallel, straight line, oscillatory motion at the seabed. For each cycle of the oscillatory motion, a time-dependent boundary layer develops over the bed, the wave boundary layer. In addition to applications in coastal engineering, oscillatory boundary layers exist in several other fields such as biological flows and turbomachinery. With the pioneering work of Lundgren & Jonsson (1961), wave boundary layers have been the subject of much investigation in the past two decades or so (see, for example, Hino, Sawamoto & Takasu 1976; Hino *et al.* 1983; Kemp & Simons 1982, 1983; Sleath 1987; Jensen, Sumer & Fredsøe 1989; Lodahl, Sumer & Fredsøe 1998; Dixen *et al.* (2008) on the experimental side and Grant & Madsen 1979; Fredsøe 1984; Justesen 1988; Vittori & Verzicco 1998; Costamagna, Vittori & Blondeaux 2003; Lohmann *et al.* 2006; Salon, Armenio & Crise 2007; Fornarelli & Vittori 2009 on the theoretical side). Major reviews on the subject have been presented by Soulsby *et al.* (1993), Blondeaux & Vittori (1999) and Sumer (2003), and, although

---

† Present address: DHI, Agern Alle 5, 2970 Hørsholm, Denmark.
‡ Email address for correspondence: bms@mek.dtu.dk

not to the extent of the latter three reviews, in several papers published in recent years, Fredsøe *et al.* (2003), Salon *et al.* (2007), Dixen *et al.* (2008) and Fuhrman, Fredsøe & Sumer (2009*a*, 2009*b*).

Of particular interest is the transition to turbulence. Turbulence first emerges in the form of spikes in the wall shear stress signal (or in the near-wall velocity signal) prior to the flow reversal near the wall (Hino *et al.* 1976; Jensen *et al.* 1989; Lodahl *et al.* 1998). (These spikes can be seen in figure 14.) Kemp & Simons (1982) noted high turbulence in the decelerating stage of the oscillatory motion. Similar behaviour in the streamwise component of the velocity accompanied with violent fluctuations in the cross-stream and spanwise velocities near the wall was observed in the direct simulations of transition in oscillatory boundary layers (achieved by direct numerical simulation, DNS) in the study of Vittori & Verzicco (1998). Their figure 6 is an excellent demonstration of these features where what they call perturbations of the Stokes flow start to appear towards the end of the accelerating phases of the cycle and are sustained during part of the decelerating phases. They also note that the turbulent velocity fluctuations increase in strength, and the decelerating part of the cycle during which they are observed becomes longer. There is quite a substantial amount of literature on the topic of transition to turbulence in oscillatory boundary-layer flows. Akhavan, Kamm & Shapiro (1991*a*, 1991*b*), Blondeaux & Vittori (1994), Lodahl *et al.* (1998), Vittori & Verzicco (1998), Costamagna *et al.* (2003), Blennerhassett & Bassom (2006) and Tuzi & Blondeaux (2008) can be consulted for recent, as well as earlier, theoretical and experimental work on the subject.

Jensen *et al.* (1989) and Lodahl *et al.* (1998) interpreted the transition to turbulence in terms of the combined effect of two factors: (*a*) The adverse pressure gradient prior to the flow reversal near the wall becomes relatively large; and (*b*) The near-wall velocities become relatively small at this stage. These two effects combined presumably lead to a favourable environment for the inception of turbulence. However, some researchers (e.g. Foster, Holman & Beach 1994; Foster 1997) have suggested that turbulence is caused by an inflectional-point shear layer instability, as the phase-resolved velocity profiles immediately after the near-wall flow reversal develop inflectional-point instabilities. The inflectional-point instability and the controversy it caused was brought into focus already in 1991 by Akhavan *et al.* (1991*b*); these authors pointed out that a quasi-steady instability analysis for an oscillatory Stokes flow predicts the most unstable profiles to occur near the start of the acceleration stage, and the most unstable eigenmodes have their peak energies around inflectional points, emphasizing that these predictions do not agree with experimental observations which show that the flow becomes explosively unstable during the deceleration stage, and also that the predicted critical Reynolds number for the former type of the instability, $(Re_\delta)_{cr} \sim 85$, is not in accord with $(Re_\delta)_{cr} \sim 500$, the critical Reynolds number associated with the transition to turbulence (the explosive instability during deceleration) observed in the experiments. Here, $Re_\delta = \delta_1 U_{0m}/\nu$ in which δ_1 is the Stokes length (10) and U_{0m} the amplitude of the oscillatory free-stream velocity. (Note that $(Re_\delta)_{cr} \sim 500$ corresponds to $(Re)_{cr} \sim 1.25 \times 10^5$, in terms of the Reynolds number adopted in this study; see (5).)

The questions that remain unsettled are: (*a*) What is the cause of the aforementioned spikes observed in the wall shear stress (or in the near-wall streamwise velocity) in transition to turbulence? (*b*) What are the parameters that govern the development of the flow features that cause the spikes? (*c*) What is the role of the inflectional point shear layer instability in the transition to turbulence in oscillatory boundary layers? Is it really the cause of the inception of turbulence? Or is the inception of turbulence
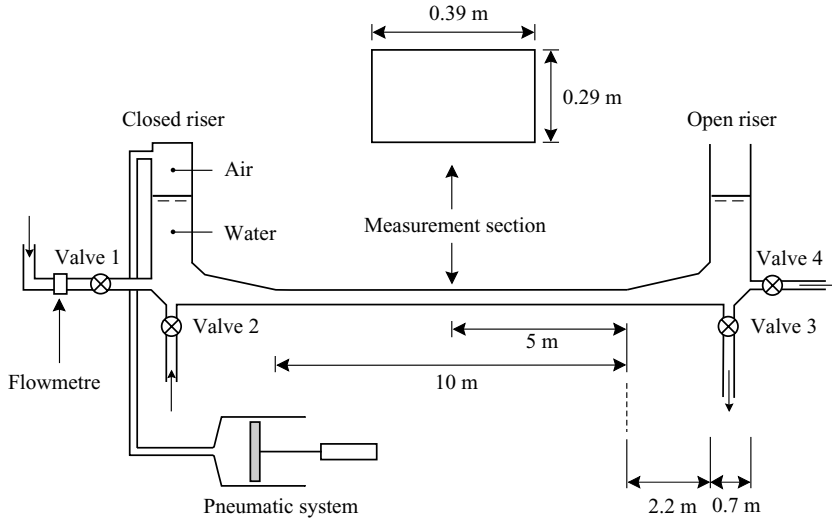
FIGURE 1. Oscillating water tunnel.

caused by something else? (*d*) What is the influence of a current superimposed on the oscillatory flow, the case of combined waves and current, an important flow environment in coastal engineering?

This study essentially addresses these questions. The combined visual and quantitative techniques reveal two significant features, which deserve early mention. First, the previously mentioned inflectional-point shear layer instability leads to generation of small vortex tubes near the wall extending across the width of the boundary layer (in the transverse direction). Second, the spikes observed in the wall-shear stress signal are caused by turbulent spots, the arrowhead-shaped flow features known from steady boundary-layer research. The inception of turbulence is shown to be associated with the emergence of the turbulent spots, similar to the laminar-to-turbulence transition in steady boundary layers. (We note that 'turbulence' generated by the previously mentioned vortex tubes has a very limited lifespan, and its magnitude is quite insignificant compared with that generated by the turbulent spots for the same Reynolds number as detailed in the paper.)

2. Experimental facility

Two experiments were conducted: pure oscillatory flow experiments and combined oscillatory flow and current experiments.

2.1. *Pure oscillatory flow experiments*

2.1.1. *The oscillatory-flow water tunnel and instrumentation*

The experiments were carried out in a U-shaped oscillatory-flow water tunnel (figure 1). This tunnel is the same as that described by Jensen *et al.* (1989). The working section was 10 m long, 0.29 m high and 0.39 m wide. The top and side walls were made of smooth transparent perspex plates. The bottom wall was made of smooth acrylic plates. The oscillatory flow in the tunnel was driven by an electronically controlled pneumatic system. The period of the oscillations was maintained at 9.72 s, the natural period of the oscillating water in the tunnel.
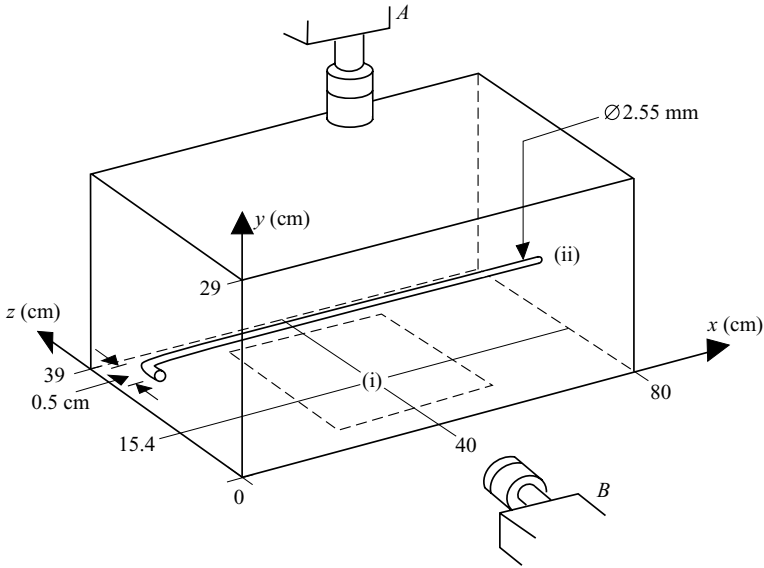
FIGURE 2. Test setup. (*a*) Hot-film probe. (*b*) Dye tube.

Two measurements were made: bed shear stress measurements and free-stream velocity measurements.

The bed shear stress was measured with a Dantec 55R46 hot-film probe, mounted flush to the bottom wall in the middle of the measurement section (figure 2, symbol (i)). The hot-film probe has a hot-film sensor, the key element of the probe, inserted in a quartz rod housed in a 2.1 mm diameter chromium-plated brass cylinder element. The dimensions of the hot-film sensor were $(d_x \times d_z) = (0.2\,\text{mm} \times 0.75\,\text{mm})$. In order to ensure correct calibration, the hot-film probe was calibrated *in situ* where the calibration coefficients A and B in the calibration relation

$$\tau_0^{1/3} = AE^2 + B \tag{1}$$

were determined in oscillatory laminar boundary-layer conditions for which the theoretical solution for the wall shear stress is known (as done by Jensen *et al.* 1989). Here E is the voltage drop. The temperature field in the water in the calibration tests was practically the same as that in the actual experiments. (The water temperatures are given in the captions of tables 1 and 2.) In this context, we note that a static calibration is not necessarily the same as a dynamic one as the temperature field in the substrate may change during a static calibration. This is especially true for hot films measuring in air but may also be important in liquids.

For turbulent flows, (1) (with the coefficients A and B determined from laminar-flow experiments) holds true provided that τ is the instantaneous value of the wall shear stress and E the corresponding instantaneous voltage drop (Hanratty & Campbell 1983).

The free-stream velocity, which acted as a reference signal, was measured with a one-component laser doppler anemometer (LDA), used in forward scatter mode. The LDA was a Dantec LDA 04 system equipped with a 15 mW He–Ne laser, a Dantec 55N10 frequency shifter and a Dantec 55N20 frequency tracker. The measurement point was located at the centre line, at the point $(x, y, z) = (20\,\text{cm}, 14.5\,\text{cm}, 19.5\,\text{cm})$ (figure 2). The measurement point was not exactly at the same section as the wall

shear stress probe. This was to avoid the laser beams blocking the viewing areas of the cameras used in the flow visualization (figure 2, Cameras A and B). The sampling interval for the hot film and velocity measurements was 13.3 ms.

2.1.2. *Flow visualization*

Two types of flow visualizations were performed: plan-view flow visualization (Camera A) and side-view flow visualization (Camera B). Because of the experimental constraints, these tests were conducted not at the same time, but separately. A Panasonic GP-KS162 industrial colour CCD digital micro camera was used in the tests. The camera produces 25 frames per second; thus, with the given oscillatory-flow period, $T = 9.72$ s, which yielded 243 frames per period (or an increment in phase between consecutive frames of $\Delta(\omega t) \approx 1.5°$). This time resolution was small enough to follow the time evolution of coherent, organized flow structures observed in the present experiments.

Plan-view flow visualization. The thin-layered milk technique developed by Hayashi & Ohashi (1982) was used in the tests. Skimmed milk diluted with water at a ratio of 1:9 was coloured by adding a small amount of ordinary red food colour, hereafter referred to as 'dye'. The bottom of the tunnel was white. This made it relatively easy to identify and interpret coherent structures made visible by the dye. (The shadows of the lifted coherent structures, made visible by the dye, were quite distinct against the white background.) The dye was injected through a small pipe situated at the junction between the bottom and the sidewall (figure 2). Prior to injection, the dye had been cooled to a temperature around 5°C. At this temperature the density of water is close to its maximum so that the dye remains in a thin layer at the bottom (of a thickness of less than 1 mm). In order to avoid density gradients due to temperature differences, the dye was, after injection, allowed to reach the same temperature as the surrounding water before the experiment was conducted. Furthermore, the density of the dye was kept close to that of water, and well below the critical value for stable stratification to occur (Carstensen 2006). Illumination was through the top wall of the measurement section of the tunnel.

In the tests, (*a*) the bed shear stress and free-stream velocity measurements, and (*b*) the plan-view flow visualization were synchronized. The synchronization was achieved by a light-emitting diode. The diode was set to flash at each zero crossing of the free-stream velocity while simultaneously a synchronization signal was sent to the data acquisition system which recorded the bed shear stress and the free-stream velocity. As both the data acquisition system and the video recording were operated at constant sampling frequencies, a linear relation between the frame number of the flow visualization and the sample number of the data acquisition was established to relate the video recording to the sampled velocity and bed shear-stress signals.

In an exploratory test series conducted before the actual tests, it was evident that the dye, introduced into the water in a thin layer at the bottom, which remained at rest until the water was set in motion, lasted over a fairly long period of time under laminar-flow conditions (as long as up to about ten cycles of the motion, $O(100$ s), or more). This was not the case, however, for turbulent conditions where the dye was dispersed extremely rapidly, within the first two or three cycles after transition to turbulence had occurred. This limited the duration of some of the tests to the first three or four cycles of the motion where the water was set into motion from rest, with the amplitude being increased steadily throughout the test (figure 3*a*).
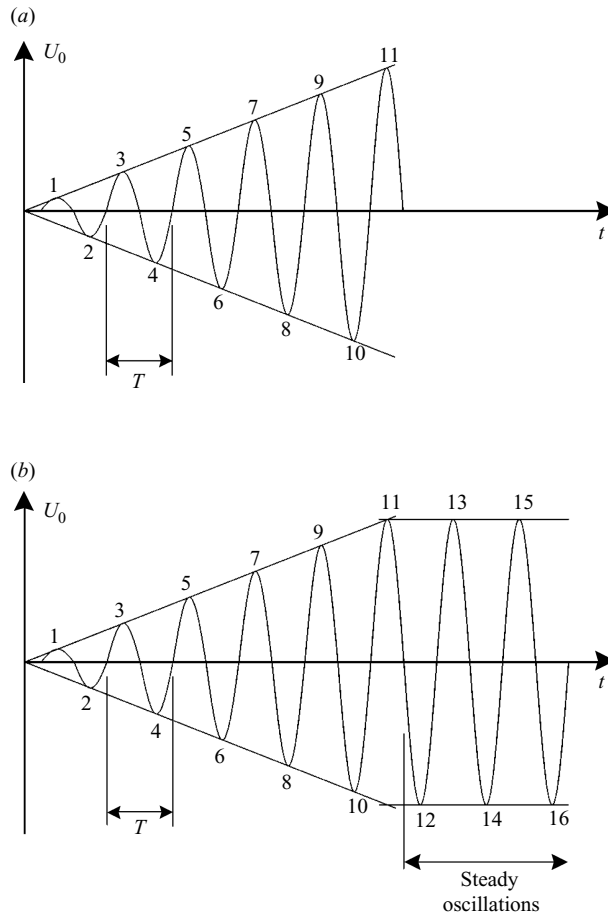
FIGURE 3. (*a*) Free-stream velocity in the experiments except in test 2.
(*b*) Free-stream velocity in test 2.

The following procedure was adopted in the tests: (*a*) Release the dye when the water is at rest; (*b*) Make sure that the bottom area where the dye spreads well coincides with the viewing area of the camera; (*c*) Start the video recording and data sampling shortly before the water is set into motion from rest; (*d*) Videotape the flow, and sample the bed shear stress and the free-stream velocity data as the amplitude of the oscillatory motion is increased steadily as illustrated in figure 3(*a*), and continue to do so until the dye is completely dispersed (dispersed so much so that the flow visualization becomes practically impossible); and (*e*) Continue the data sampling until the end of the test.

In one test (test 2), the amplitude was increased steadily for the first eleven half-cycles (as in figure 3*a*), and then kept constant thereafter over the next five half-cycles (the steady-oscillations portion of the motion in figure 3*b*). The amplitude of the motion in this test was relatively small, and therefore the dye 'survived', enabling the flow visualization for this latter part of the motion to be materialized.

Regarding the question how the present oscillatory flow (where the amplitude increases steadily; figure 3*a*) compares with steady oscillatory flow (where the
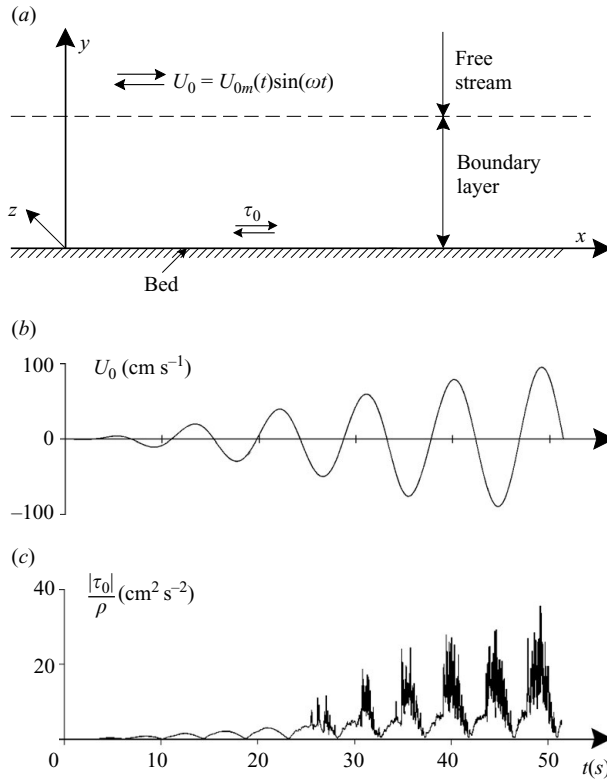
(a)

(b)

(c)

FIGURE 4. Traces of the bed shear stress and the free-stream velocity. Test 9.

amplitude remains constant), the friction factor and the phase lead of the bed shear stress, two most important quantities to describe the oscillatory boundary-layer flow, have been worked out, and compared with the classic steady oscillatory flow data in the Appendix (figure 21). This shows that the two sets of data are in good agreement. The Appendix gives a detailed discussion regarding this issue.

Figure 4 shows sample records (test 9, see table 1), the top time series representing the free-stream velocity, U_0, and the bottom time series the bed shear stress, τ_0. (Note that the hot-film bed shear stress probe does not sense the direction of the bed shear stress and, therefore, the bed shear stress does not change sign as the free-stream flow alternates between positive and negative directions.)

Side-view flow visualization. This was achieved, using fluorescent dye and a vertical laser sheet, which was 1 mm in thickness. The laser sheet was placed so that the area just above the flush mounted hot film was illuminated. (The fluorescent dye was selected in favour of the coloured milk in these tests. This was because the milk blocked the viewing area of the camera, Camera B, the area illuminated by the laser sheet and, therefore, no clear visualization could be achieved.) The fluorescent dye was cooled, injected and allowed time to gain the same temperature as the surrounding water, in the same way as in the plan-view flow visualization tests. Similar to the plan-view flow visualization measurements, the bed shear stress and free-stream velocity measurements were synchronized with the flow visualization in these tests, too.

Test no. (1)	Total of runs (2)	Half-cycles videotaped and/ or measured (see figure 3 for the definition sketch) (3)	U_{0m} (cm s^{-1}) (4)	$a = U_{0m}T/(2\pi)$ (cm) (5)	$Re = U_{0m}a/\nu$ (6)	Flow visualization: plan view or side view (7)
		(1) Flow visualization synchronized with bed shear stress and free-stream velocity measurements				
1	1	1–11	0.0–21.1	0.0–32.6	5.3×10^2–6.9×10^4	Plan view
2	2	1–16	0.6–33.0	0.9–51.0	1.1×10^2–1.7×10^5	Plan view
3	2	1–11	1.5–44.2	2.3–68.4	3.5×10^2–3.0×10^5	Plan view
4	2	1–9	2.3–49.8	3.5–77.0	7.8×10^2–3.9×10^5	Plan view
5	2	1–6	5.0–53.7	7.7–83.1	3.3×10^3–4.3×10^5	Plan view
6	2	1–5	8.7–70.8	13.5–109.5	1.1×10^4–7.5×10^5	Plan view
7	2	1–4	10.7–62.1	16.5–93.0	1.7×10^4–6.0×10^5	Plan view
8	1	1–4	14.8–75.2	22.9–116.3	3.4×10^4–8.7×10^5	Plan view
9	1	1–6	4.4–49.3	6.8–76.2	3.0×10^3–3.8×10^5	Side view
10	1	1–9	1.8–47.5	2.8–73.5	5.0×10^2–3.5×10^5	Side view
		(2) Bed shear stress and free-stream velocity measurements (Dye was diluted to the extent that no flow visualization was possible)				
4	2	10–11	55.8–61.0	86.3–94.3	4.8×10^5–5.8×10^5	–
5	2	7–11	64.5–102.4	99.8–158.4	6.4×10^5–1.6×10^6	–
6	2	6–11	83.9–156.4	129.7–242.0	1.1×10^6–3.8×10^6	–
7	2	5–11	79.8–177.1	123.5–273.5	9.9×10^5–4.9×10^6	–

TABLE 1. Test conditions. Pure oscillatory flow. Period of the motion, $T = 9.72$ s. Video recording, bed shear stress and free-stream velocity measurements were synchronized. Water temperature was 20°C and the kinematic viscosity was 0.010 cm^2 s^{-1}.

Samples of flow visualizations, both in plan view and in side view, can be seen in supplementary movies 1–4 at journals.cambridge.org/flm.

2.2. Combined oscillatory flow and current experiments

A constant head tank, the head being 6 m with respect to the mean water level in the tunnel, provided the current. The desired flow rate was obtained by simultaneous adjustments of the inlet and outlet valves of the tunnel. The current flow rate was measured by a magnetic flowmeter installed on the supply pipe before the pipe enters the tunnel (figure 1). (This setup to generate current in the tunnel was essentially the same as that used by Lodahl *et al.* 1998.)

The following procedure was adopted in the tests. The dye for the flow visualization was injected while the oscillatory component of the combined flow was nil, and the current component was rather small (regulated by valves 1 and 3; figure 1). Once the dye was injected, first the current component of the combined flow was adjusted to the desired value of the flow rate, Q (see table 2), and then the oscillatory flow component was added. The current was adjusted using valves 2 and 4. These two valves were electronically controlled to open gradually at small increments. The gradual increase was adopted in favour of sudden increase to avoid setting the water in the tunnel into natural oscillations and to allow the steady boundary layer to develop before the oscillatory component was added.

The sampling interval for the hot film and velocity measurements was 12.5 ms.

Test no.	Half-cycles videotaped and measured	U_{0m} (cm s^{-1})	$a = U_{0m}T/(2\pi)$ (cm)	$Re = U_{0m}a/\nu$	Q (l s^{-1})	$V = Q/(bh)$ (cm s^{-1})	$Re_c = 4R_hV/\nu$
(1)	(2)	(3)	(4)	(5)	(6)	(7)	(8)
11	1–11	−32.9	−50.8	-1.7×10^5	1.56	1.4	4.5×10^3
12	1–11	0.9–42.3	1.4–65.3	1.3×10^2–2.7×10^5	1.57	1.4	4.6×10^3
13	1–9	1.7–47.9	2.6–74.0	4.5×10^2–3.5×10^5	1.58	1.4	4.6×10^3
14	1–6	3.7–50.8	5.7–78.4	2.1×10^3–3.9×10^5	1.59	1.4	4.6×10^3
15	1–5	6.9–68.4	10.7–105.6	7.4×10^3–7.2×10^5	1.59	1.4	4.6×10^3
16	1–4	8.4–56.4	13.0–87.1	1.1×10^4–4.9×10^5	1.60	1.4	4.6×10^3
17	1–11	−33.9	−52.4	-1.8×10^5	3.74	3.3	1.1×10^4
18	1–11	1.0–43.1	1.5–66.6	1.5×10^2–2.8×10^5	3.71	3.3	1.1×10^4
19	1–9	1.9–47.7	3.0–73.7	5.7×10^2–3.5×10^5	3.75	3.3	1.1×10^4
20	1–6	4.2–54.0	6.5–83.4	2.7×10^3–4.5×10^5	3.71	3.3	1.1×10^4
21	1–5	7.3–66.3	11.3–102.4	8.2×10^3–6.7×10^5	3.69	3.3	1.1×10^4
22	1–4	8.6–58.3	13.3–90.1	1.1×10^4–5.2×10^5	3.79	3.4	1.1×10^4
23	1–11	−21.0	−32.4	-6.7×10^4	5.98	5.3	1.7×10^4
24	1–11	−33.3	−51.4	-1.7×10^5	5.97	5.3	1.7×10^4
25	1–11	0.9–42.2	1.4–65.1	1.2×10^2–2.7×10^5	5.95	5.3	1.7×10^4
26	1–8	1.5–41.7	2.3–64.3	3.5×10^2–2.7×10^5	5.98	5.3	1.7×10^4
27	1–6	4.3–51.3	6.6–79.2	2.8×10^3–4.0×10^5	5.94	5.3	1.7×10^4
28	1–4	6.9–50.5	10.6–77.9	7.2×10^3–3.9×10^5	5.91	5.2	1.7×10^4
29	1–4	9.5–57.7	14.7–89.1	1.4×10^4–5.1×10^5	6.01	5.3	1.8×10^4
30	1–11	−22.2	−34.3	-7.2×10^4	7.95	7.0	2.2×10^4
31	1–11	−35.8	−55.3	-1.9×10^5	8.09	7.2	2.2×10^4
32	1–11	0.9–44.9	1.4–69.3	1.3×10^2–2.9×10^5	8.00	7.1	2.2×10^4
33	1–9	1.8–48.7	2.8–75.3	4.8×10^2–3.5×10^5	8.00	7.1	2.2×10^4
34	1–6	3.7–54.1	5.8–83.6	2.0×10^3–4.3×10^5	7.97	7.0	2.2×10^4
35	1–4	8.3–49.6	12.8–76.6	1.0×10^4–3.6×10^5	8.00	7.1	2.2×10^4
36	1–4	10.5–60.0	16.3–92.7	1.6×10^4–5.3×10^5	7.97	7.0	2.2×10^4
37	1–11	−20.8	−32.2	-6.3×10^4	9.87	8.7	2.7×10^4
38	1–11	−34.7	−53.6	-1.7×10^5	9.88	8.7	2.7×10^4
39	1–11	0.9–45.7	1.4–70.5	1.2×10^2–3.0×10^5	9.89	8.7	2.7×10^4
40	1–9	1.6–48.9	2.4–75.5	3.5×10^2–3.5×10^5	9.90	8.8	2.7×10^4
41	1–6	4.2–52.5	6.5–81.1	2.5×10^3–3.5×10^5	9.83	8.7	2.7×10^4
42	1–4	7.6–50.4	11.7–77.9	8.3×10^3–3.7×10^5	9.88	8.7	2.7×10^4
43	1–4	9.8–57.1	15.1–88.2	1.4×10^4–4.7×10^5	9.81	8.7	2.7×10^4

TABLE 2. Test conditions. Combined oscillatory flow and current. Period of the motion, $T = 9.7$ s. Video recording, bed shear stress and free-stream velocity measurements were synchronized. For tests 11–29, water temperature was 19.5°C and the kinematic viscosity was 0.0101 cm^2 s^{-1}; for tests 30–36, the water temperature was 18.0°C and the kinematic viscosity was 0.0106 cm^2 s^{-1}; and for tests 37–43, the water temperature was 17.5°C and the kinematic viscosity was 0.0107 cm^2 s^{-1}. $b = 0.39$ m, the width of the tunnel, and $h = 0.29$ m, the height of the tunnel. No side-view flow visualization test was conducted. One run for each test.

3. Test conditions

3.1. *Test conditions for pure oscillatory flow experiments*

Table 1 summarizes the test conditions for the pure oscillatory flow experiments. Note that U_{0m} in the table is the amplitude of the free-stream velocity defined by

$$U_0 = U_{0m}(t)\sin(\omega t) \qquad (2)$$

with $U_{0m}(t) = \alpha + \beta t$ in which α and β are constants; ω is the angular frequency

$$\omega = \frac{2\pi}{T} \tag{3}$$

and T is the period of the oscillatory motion. The quantity a in the table is the amplitude of the motion calculated from

$$a = \frac{U_{0m}T}{2\pi}. \tag{4}$$

The Reynolds number is defined by

$$Re = \frac{aU_{0m}}{\nu}. \tag{5}$$

3.2. *Test conditions for combined oscillatory flow and current experiments*

Table 2 summarizes the test conditions for combined oscillatory flow and current experiments. The quantity V in the table is the cross-sectional mean velocity of the current component of the combined flow, calculated from

$$V = Q/(bh) \tag{6}$$

where the product bh is the cross-sectional area of the measurement section (b is the width, $b = 0.39$ m, and h is the height, $h = 0.29$ m; figure 1). Re_c in the table is the current Reynolds number, defined by

$$Re_c = \frac{4R_h V}{\nu}, \tag{7}$$

where ν is the kinematic viscosity and R_h is the hydraulic radius:

$$R_h = (bh)/(2b + 2h). \tag{8}$$

4. Coherent structures

These observations show that there are essentially two kinds of coherent flow structures:

(i) *Vortex tubes.* These are basically two-dimensional vortices close to the bed extending across the width of the flow in the plan view. These features emerge when Re is $Re \gtrsim 7 \times 10^4$. (No vortex tubes were observed, on the other hand, for Re larger than 3×10^5 in the present tests.)

(ii) *Turbulent spots.* These are isolated areas close to the bed in an otherwise laminar boundary layer (in space and phase) where the flow 'bursts' with violent oscillations. These features emerge when $Re > 1.5 \times 10^5$. The emergence of the turbulent spots marks the onset of turbulence as detailed below.

Each flow structure is now considered individually. Note that, in the following description, the phase $\omega t = 0°$ corresponds to the zero upcrossing of the free-stream velocity signal (2) and, therefore, $\omega t = 0°$–$180°$ corresponds to one half-cycle and $\omega t = 180°$–$360°$ to the following half-cycle of the motion.

4.1. *Vortex tubes*

4.1.1. *General description*

In the plan view, these features appear as a series of transverse bands with alternating concentration of dye (figure 5; see also supplementary movie 1). (In
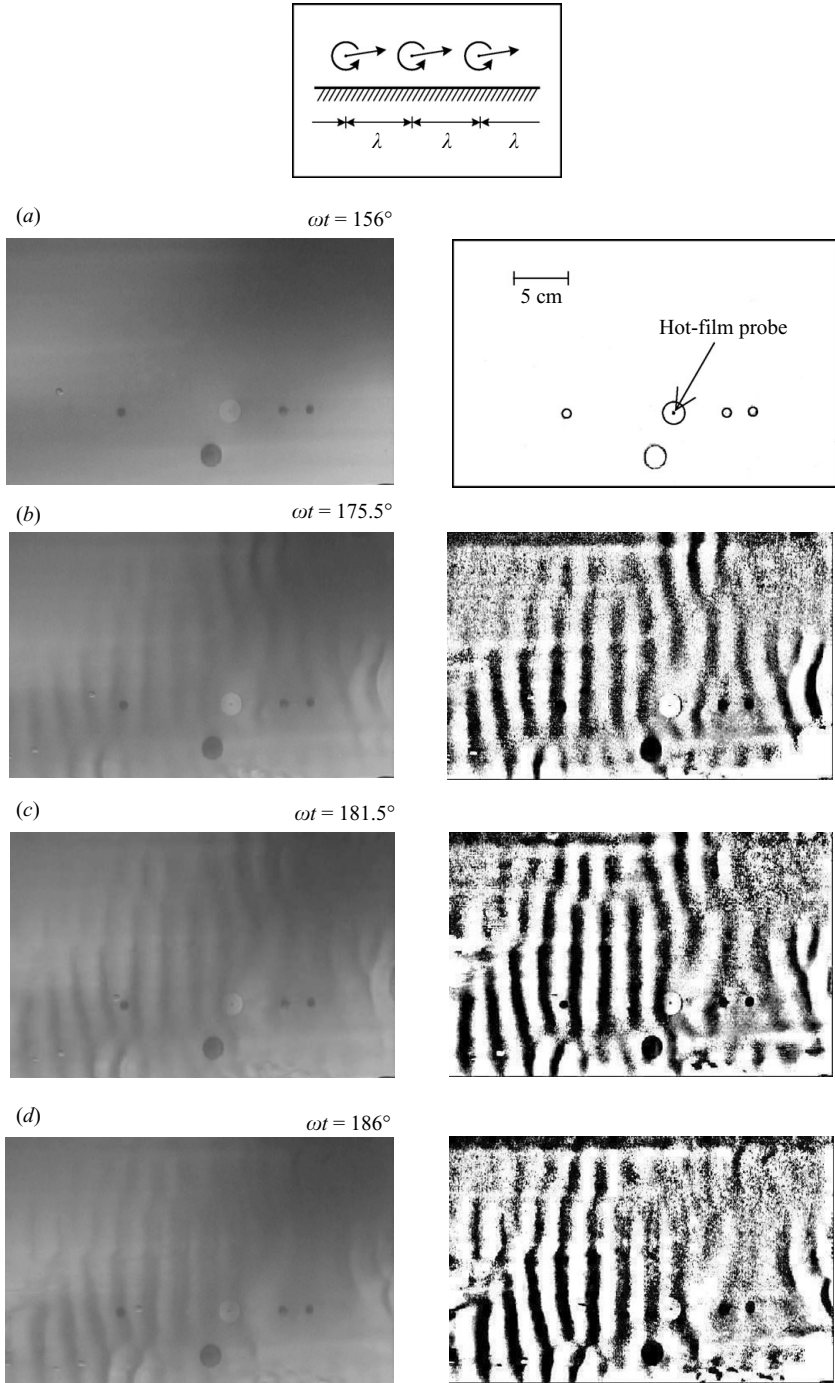
FIGURE 5. Time evolution of vortex tubes (plan view). Test 5, half-cycle 5. $Re = 2.9 \times 10^5$. The flow near the bed (where the vortex tubes are located) is from left to right and, therefore, the system of vortex tubes is in constant motion from left to right throughout the sequence (*b*)–(*d*). (Inset) The side view of the vortex tubes.

connection with the plan-view video frames presented in figure 5 and detailed in the text, we note that the four circular, black spots seen in figure 5 are actually plastic dummy probes mounted flush to the bottom of the tunnel. Special care was taken to ensure that no disturbance was introduced to the flow by these dummy probes.)

Vortex tubes first emerge when the flow Reynolds number is $Re \simeq 7 \times 10^4$, as mentioned above. The sequence of video frames shown in figure 5 illustrates the time development of the vortex tubes in the plan view. The video frames are accompanied by sketches, which are essentially direct copies of the video frames where the contrast is grossly enhanced to aid the reader. The Reynolds number of the test is $Re = 2.9 \times 10^5$. The flow direction in the *free-stream velocity* is from right to left in figure 5(a, b) and in the opposite direction in figure 5(c, d), while the *flow near the bed* (where the vortex tubes are located) is from left to right throughout the sequence (figure 5a–d). The vortex tubes in this test first emerged at the phase value of about $\omega t = 165°$. They grew stronger (figures 5b and 5c) as they were convected in the near-bed flow direction (from left to right in the figure). They were strongest at $\omega t = 186°$ beyond which they gradually lost coherence and eventually disappeared ('died') at $\omega t = 225°$ (i.e. 45° into the following half-cycle). The vertical scale of these structures is much smaller, $O(5\,\text{mm})$ than the spacing between two neighbouring tubes λ, $O(20\,\text{mm})$.

These vortex tubes are the result of inflectional-point shear layer instability. For $\omega t > 135°$ (i.e. from the instant of the near-bed flow reversal), the laminar oscillatory flow velocity profile (e.g. Batchelor 1967)

$$\frac{u(y, t)}{U_{0m}} = \sin(\omega t) - \exp\left(-\frac{3\pi}{4}\frac{y}{\delta}\right)\sin\left(\omega t - \frac{3\pi}{4}\frac{y}{\delta}\right) \tag{9}$$

experiences an inflection point. Here, δ is the boundary-layer thickness defined as $y = \delta$, where the velocity becomes maximum at the phase value $\omega t = 90°$ (Sumer, Jensen & Fredsøe 1987). Note that δ is related to the Stokes length

$$\delta_1 = \left(\frac{2\nu}{\omega}\right)^{1/2} \tag{10}$$

by

$$\delta = \frac{3\pi}{4}\delta_1 = \frac{3\pi}{4}\left(\frac{2\nu}{\omega}\right)^{1/2}. \tag{11}$$

Such shear layer is unstable to small disturbances through the Kelvin–Helmholtz instability mechanism (Blondeaux & Seminara 1979; Akhavan *et al.* 1991b; Blondeaux & Vittori 1994; Costamagna *et al.* 2003), whereby the vorticity in the shear layer eventually concentrates in discrete vortices as sketched in the inset in figure 5.

The velocity induced by the vortices sweep the dye, initially situated uniformly in a thin layer over the bottom wall, into vortices. Hereby the vortices become visible as exhibited in figure 5. This figure also reveals that the described instability process is initially a two-dimensional or quasi two-dimensional process, similar to that observed in steady shear layers (e.g. Browand 1966; Bernall 1981; Ho & Huerre 1984). However, in this case, the inflection point (and the shear layer) moves constantly upwards as the boundary layer develops (as can be readily verified from (9)). The inflection point is the center of the rolled-up vortices (maximum vorticity); thus, the vortex tubes will also move away from the bed. Although not clear from the still plan-view images (e.g. figure 5), this can be seen quite clearly in the plan-view videos when played live, revealed by the shadows of the structures; see Movie 1.
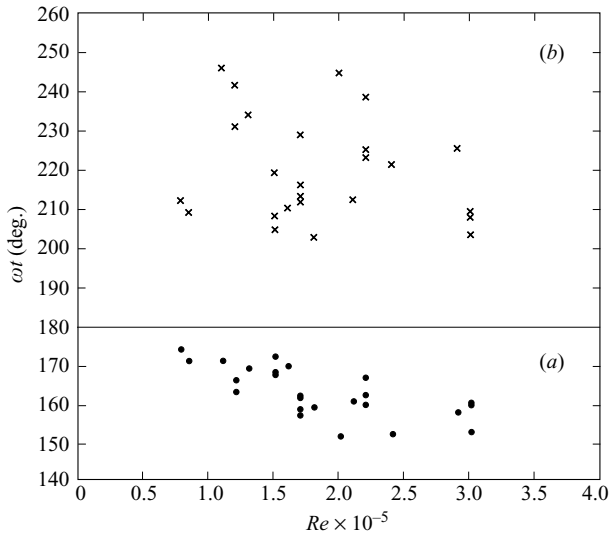
FIGURE 6. Phase values of inception (a) and disappearance (b) of vortex tubes.

In figure 6, we plot (a) the phase values at which the vortex tubes first emerge (circles) and (b) the phase values at which they disappear (crosses) for the entire set of data obtained in the present tests (table 1).

Although somewhat limited, the present data (figure 6) indicate that there is a trend that the phase where the vortex tube first emerges decreases with increasing Re (circles), while the phase values where the vortex tubes disappear (crosses) show no Reynolds number dependence. The decrease in ωt with increasing Re may be explained in terms of the large increase of the slope du/dy at the inflection point with increasing Re. (This can be readily seen from the laminar solution in (9), inserting $\delta/a = (3\pi/4)(2/Re)^{1/2}$, which is obtained from (5) and (11).) The latter means that the instability occurs at smaller and smaller values of ωt with increasing Re, as revealed by figure 6. Moreover, the fact that the phase values at which the vortex tubes disappear is independent of the Reynolds number implies that the lifespan of vortices increases with Re. This, again, may be attributed to the increase in du/dy at the inflection point with increasing Re. Clearly, the larger the value of du/dy at the inflection point, the stronger the vortices, and therefore the longer the lifespan of the vortices.

Finally, as seen from figure 6, no vortex tubes are observed for Re larger than 3×10^5. This is because, for Reynolds numbers larger than this value, the flow becomes fully developed turbulent for the phases corresponding to the inception of vortex tubes, namely $\omega t = 150°$–$160°$ (see Jensen *et al.* 1989, figure 8; and figure 10 of this paper) and, therefore, the entire concept of the inflectional-point shear layer instability breaks down, and hence no vortex tubes are generated.

4.1.2. *Bed shear stress*

Figure 7 shows five video frames from the flow visualization of test 7, half-cycle 3, illustrating the passage of vortex tubes over the hot film. The *flow near the bed* (where the vortex tubes are located) is from right to left throughout the sequence (figure 7b–e). (The reason why the near-bed flow direction is different from the sequence in figure 5 is that this sequence is taken from the other half-cycle of the
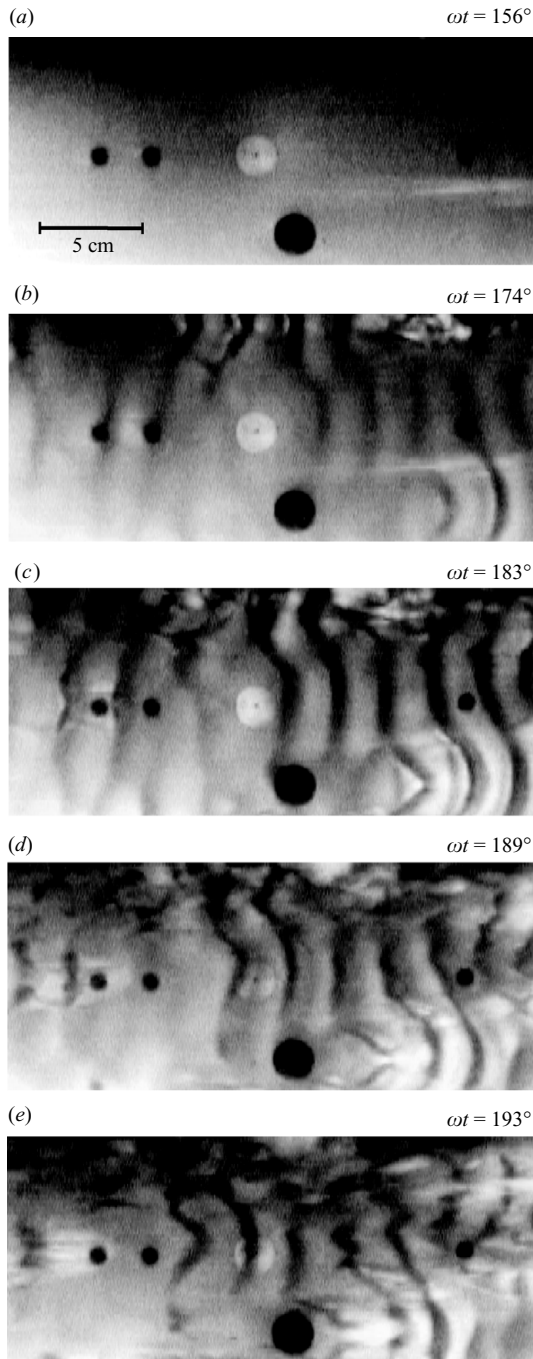
(a) $\omega t = 156°$

(b) $\omega t = 174°$

(c) $\omega t = 183°$

(d) $\omega t = 189°$

(e) $\omega t = 193°$

FIGURE 7. Vortex tubes (plan view). Test 7, half-cycle 3. $Re = 3.0 \times 10^5$. The flow near the bed (where the vortex tubes are located) is from right to left and, therefore, the system of vortex tubes is in constant motion from right to left throughout the sequence (b)–(e).

flow.) The bed shear stress time series recorded by the hot film simultaneously with the flow visualization is displayed in figure 8. At $\omega t = 156°$, the visualization shows no flow structures (figure 7a), neither does the bed shear stress (figure 8, arrow a).
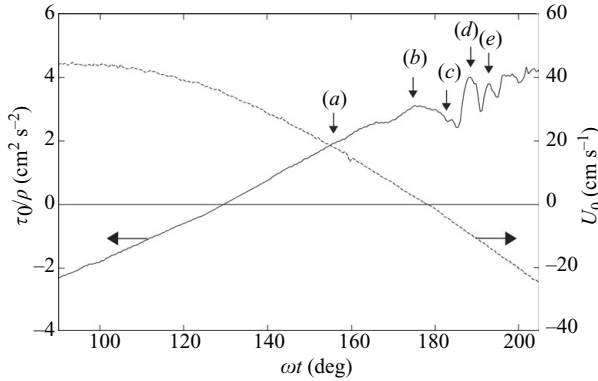
FIGURE 8. Trace of bed shear stress. The arrows (a)–(e) refer to the video frames (a)–(e) of the previous figure. Kinks in the bed shear stress signal are associated with the vortices passing over the wall shear stress probe and dips with the time periods between two successive vortices.

However, at $\omega t = 183°$, a dip in the bed shear stress is seen to correspond to the time instant between two successive vortex tubes (area represented by the absence of dye); and at $\omega t = 189°$, a kink in the bed shear stress is associated with the passage of a vortex tube just over the hot film. So, the bed shear stress is raised momentarily by the vortices passing over the wall shear stress probe while it is lowered in the time periods between two successive vortices.

The high-frequency oscillations exhibited in the bed shear stress signal in figure 8 (e.g. arrows c, d and e) may be viewed as 'turbulence'. However, this turbulence is limited to the lifetime of the vortex tubes (figure 6), and its magnitude is significantly smaller than that introduced by turbulent spots and eventually by the boundary-layer process; c.f. the magnitude of the fluctuations generated by the vortex tubes exhibited in figure 8, $O(1\,\mathrm{cm^2\,s^{-2}})$ and that generated by turbulent spots shown in figure 15$(a$–$c)$ (for the same, or even smaller Reynolds numbers, $Re \leqslant 3 \times 10^5$), $O(5$–$15\,\mathrm{cm^2\,s^{-2}})$.

It may be argued that the above-mentioned oscillations can be linked to some kind of secondary instabilities or other disturbances that develop on the top of the vortex tubes. However, this may not be the case, as these oscillations are related to the passage of successive vortex tubes over the hot film, as revealed by the present observation.

4.1.3. *Comparison with the results of others*

From the present data, it is found that the spacing between adjacent vortices λ (see the inset in figure 5), the wavelength remains practically constant throughout the vortices' lifespan. Furthermore, no correlation is found between the normalized wavelength λ/δ and the Reynolds number. From the data, the mean value of the wavelength is found to be

$$\frac{\lambda}{\delta} = 6.1 \tag{12}$$

with a standard deviation of $\sigma/\delta = 0.31$, in which the mean value and the standard deviation are calculated from a sample of the size $N = 26$. As seen, the spreading around the mean value, σ/λ, is rather small, $\sigma/\lambda = 0.05$, and may be attributed to uncertainties involved in the measurements.

Blondeaux & Vittori (1994) studied transition in oscillatory boundary layers, using a linear-stability analysis where the results of an earlier stability analysis (Blondeaux &

Seminara 1979) were also summarized. In Blondeaux & Seminara (1979), it was shown that

(i) The wavelength of the most unstable two-dimensional disturbance (a two-dimensional Tollmien–Schlichting wave which is generated by the instability of the oscillatory boundary layer) is

$$\frac{\lambda}{\delta} = 5.33 \qquad (13)$$

(figure 2 of Blondeaux & Seminara 1979), which was later confirmed by the spectral solution of the Orr–Sommerfeld equation of Akhavan *et al.* (1991*b*) and the DNSs of Navier–Stokes (N-S) equations of Costamagna *et al.* (2003); and

(ii) The vortex tubes should emerge close to the flow reversal.

The present results ((12) and figure 6*a*) agree with the above results of the stability analysis of Blondeaux & Seminara (1979).

As mentioned in the preceding paragraph, Costamagna *et al.* (2003) performed DNSs of the N-S equations and investigated the flow by means of flow visualizations and quantitative analysis of the velocity and vorticity fields. Their flow visualization clearly reveals the vortex tubes (figures 6, 7 and 9 of Costamagna *et al.* 2003). The phases of inception and disappearance of the vortex tubes (implied by their figure 8) are also consistent with the present findings (figure 6). Furthermore, the development of perturbations in the transverse direction (figure 9 of Costamagna *et al.* 2003) appears to be quite similar to those observed in the present experiments (figures 5 and 7).

Hayashi & Ohashi (1982) observed the presence of spanwise bands alternating between high and low concentration of dye in an oscillatory boundary-layer flow. Although termed *disturbances* in the original publication (and no discussion regarding their origin), the structures observed by these authors are apparently vortex tubes, similar to those in the present study. From the sequence of the plan-view photographs, the wavelength of these features is found to be $\lambda/\delta = 5.4$, which is in fairly good agreement with the present result (12). The test conditions for the Hayashi and Ohashi experiment were: the maximum value of the velocity, $U_{0m} = 49.2\,\mathrm{cm\,s^{-1}}$, the period, $T = 13.0\,\mathrm{s}$, the Reynolds number $Re = 3.8 \times 10^5$ and the boundary-layer thickness, $\delta = 0.6\,\mathrm{cm}$. Their Reynolds number ($Re = 3.8 \times 10^5$) is apparently somewhat larger than the largest Reynolds number for which the vortex tubes were observed in the present study. No clear explanation has been found for this discrepancy.

Das & Arakeri (1998) performed unsteady flow experiments in a circular pipe except in a few experiments where a channel with rectangular cross-section was used. The flow was not an oscillatory flow; rather it was an unsteady flow with the time variation of velocity having a trapezoidal shape. They used water as the working fluid and employed the fluorescent dye technique for an extensive flow visualization study. Although the flow environment was different from the present one and the flow was also not a sinusoidally oscillating flow, flow structures similar to the present vortex tubes were observed by Das and Arakeri's work for the phase values after the velocity profiles began to experience an inflection point following the flow reversal near the wall. From their experiments, Das & Arakeri gave the wavelength normalized by the average boundary layer thickness $\bar{\bar{\delta}}$ as

$$\frac{\lambda}{\bar{\bar{\delta}}} = 3.0 \qquad (14)$$

with standard deviation 0.4 for a range of the boundary-layer-thickness Reynolds number of 500–2600. (The average boundary-layer thickness is defined as that
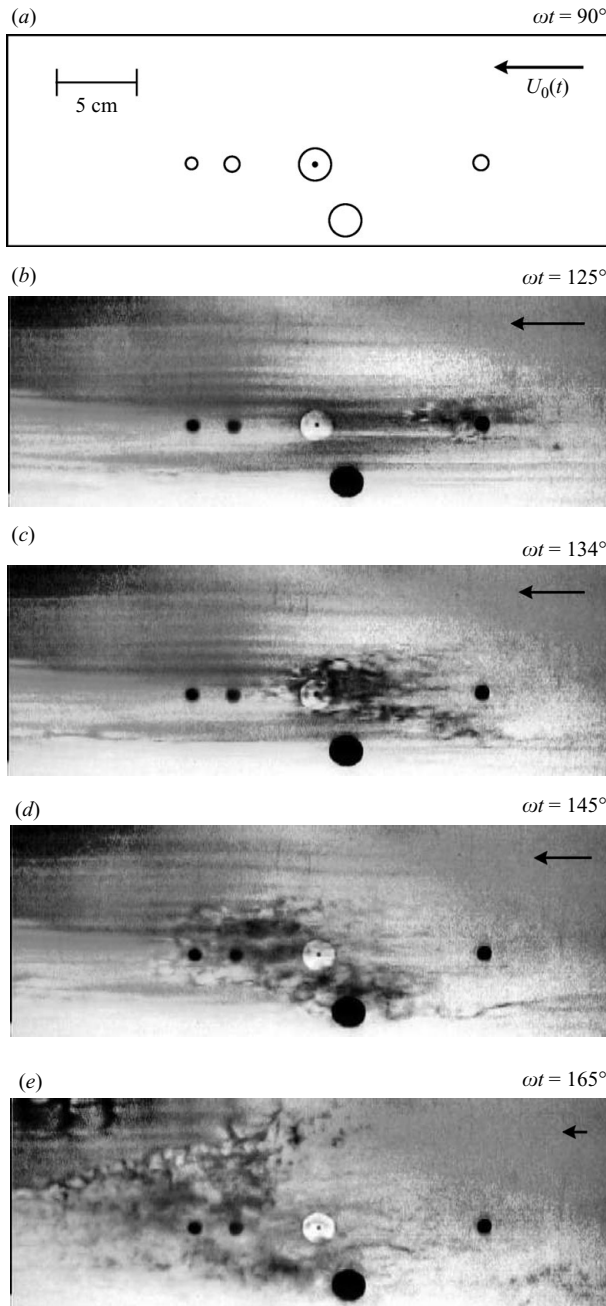
FIGURE 9. Sequence of video frames illustrating the time development of a turbulent spot.
Test 6, half-cycle 4. $Re = 4.5 \times 10^5$.

averaged over the time between t_1 and t_p in which t_1 is the instant where the flow begins to decelerate, and t_p is that where what Das & Arakeri call a perceptible wave appears.) Similar to the present findings, no Reynolds number dependence is observed in the data of Das & Arakeri. Boundary-layer flow in a pipe is governed by not only the Reynolds number but also the radius-to-boundary-layer-thickness ratio,

R/δ_1 (Lodahl *et al.* 1998). Although the range of the latter parameter is not mentioned explicitly in Das & Arakeri (1998) in relation to (14), it is inferred from their table 1 that this parameter is $R/\delta_1 = O(1-5)$, a range where R/δ_1 should play a significant role (Lodahl *et al.* 1998). Nevertheless, the wavelength found in the study of Das & Arakeri is not significantly different from that obtained by the present experiments (see (12)), considering the difference in the definition of the boundary-layer thickness.

Hino *et al.* (1983) carried out oscillatory air flow experiments in a rectangular duct including flow visualization, using the smoke technique. No detailed information is given regarding the shear-layer instability and resulting vortices in Hino *et al.* (1983). Nevertheless, they note that 'small and weak vortices are occasionally generated owing to the flow instability at the velocity inflection point'.

Sarpkaya (1993) conducted oscillatory flow experiments over a cigar-shaped body placed in an oscillating water tunnel, the oscillations being in the direction along the length of the body. The length-to-diameter ratio of the body was such that the results converge to those for an oscillatory boundary-layer over a flat plate. An extensive series of flow visualization was carried out, using the fluorescent-dye technique and a laser-sheet system. Flow processes were videotaped over a broad range of the Reynolds number, covering *Re* from $\sim 1 \times 10^5$ to $\sim 1.6 \times 10^6$. Although not specifically identified by Sarpkaya as inflection-point-instability-induced vortices, the vortices exhibited in some of the sequences and still video frames (Sarpkaya 1993; the video sequence in figure 11 and still pictures from video recording given in figure 12) resemble strikingly those observed in the present study and in the study of Das & Arakeri (1998). We should also note that the phase of inception, the phase of disappearance and the *Re* number for which these vortices were observed are all consistent with the present findings.

4.2. *Turbulent spots*

4.2.1. *General description: formation and evolution of turbulent spots*

Turbulent spots are isolated areas close to the bed, in an otherwise laminar boundary-layer flow, similar to those in steady boundary layers (first observed by Emmons 1951). The flow in these isolated areas 'bursts' with violent oscillations. Figure 9 shows a sequence of video frames, illustrating the time development of a turbulent spot in plan view (see also supplementary movie 2).

The sequence of video frames is taken from the flow visualization obtained in test 6, half-cycle 4, where $Re = 4.5 \times 10^5$. The flow is from right to left. At the phase value $\omega t = 125°$ (figure 9*b*) the spot, an arrowhead-shaped flow feature, which first emerged at an earlier phase, is seen to the right of the video frame. It travels to the left as it grows in size during the course of the half-cycle (figure 9*b*–*e*). Its lifetime comes to an end by the time the flow reverses inside the spot. With this, the spot is 'destructed' whereby it turns into an incoherent field of 'background' turbulence as the boundary layer progresses into the next half-period of the motion. (Note that the flow outside the spot reverses not at the same time but somewhat earlier.) The present observations show that the flow reversal inside the spot occurs at approximately $\omega t = 170°$ (on average), a phase value larger than that for the laminar boundary-layer reversal, $\omega t = 135°$. The delay in the flow reversal is due to turbulence inside the spot (the near-bed flow is supplied with momentum-rich fluid continuously from the outer flow due to turbulence, and this delays the flow reversal inside the turbulent spot), similar to fully developed turbulent oscillatory boundary-layer flows (Hino *et al.* 1983; Fredsøe 1984; Spalart & Baldwin 1987; Jensen *et al.* 1989). Supplementary movie 3
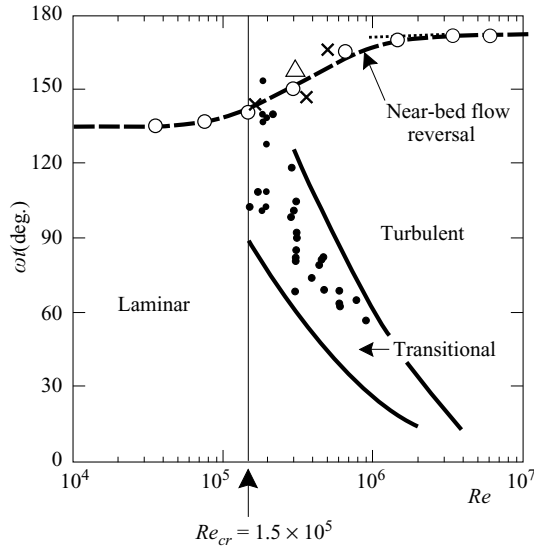
FIGURE 10. Phase of inception of turbulent spots as function of Re. Solid curves show borderlines between laminar, transitional and turbulent regions (Jensen *et al.* 1989, figure 8, obtained through the bed shear stress measurements). Dashed curve shows data corresponding to the phase values at which the near-bed flow reverses, including Hino *et al.* (1983, triangle), Jensen *et al.* (1989, empty circles), Spalart & Baldwin (1987, crosses) and Fredsøe (1984, dotted line). Near-bed flow reversal occurs at $\omega t = 135°$ in the laminar regime, and approximately at $170°$ (as $Re \rightarrow 10^7$) in the turbulent regime.

illustrates the time development of turbulent spot in side view (see also Carstensen 2006). We note that the vertical extent of the turbulent spot in the test was $O(10\,\text{mm})$.

Spots videotaped in the plan-view flow visualization are grouped in two categories: (*a*) spots that are generated (and therefore first emerge) inside the viewing area (figure 2); and (*b*) those that are not generated inside this area, but travel across it. Data regarding the phase of emergence of the first-category spots are plotted in figure 10 (filled circles). In the same figure, two other sets of data also are plotted:

(i) Data corresponding to the borderlines between three different regimes (laminar, transitional and turbulent) of boundary-layer flows, the thick solid curves, taken from Jensen *et al.* (1989, figure 8).

(ii) Data corresponding to the phase values at which the near-bed flow reverses (the dashed curve). This curve represents the experimental data of Jensen *et al.* (1989, empty circles) and Hino *et al.* (1983, triangle); a set of numerical results of Spalart & Baldwin's (1987) direct N-S simulations for transitional boundary layers (crosses); Fredsøe's (1984) theoretical solution for fully developed turbulent boundary layers (dotted line); and the classic laminar solution $\omega t = 135°$. (Note that Sarpkaya 1993 made an extensive comparison of his own experimental data with the near-bed-flow-reversal data plotted in figure 10, and found that all data coincide.)

First of all, no spots are observed for the Reynolds number smaller than $(Re)_{cr} = 1.5 \times 10^5$. For Re smaller than this critical value, the flow remains laminar (except in the cases where the previously mentioned vortex tubes come into existence as a result of the hydrodynamic instability caused by the inflection point in the velocity profile). The critical value of the Reynolds number, $(Re)_{cr} = 1.5 \times 10^5$, appears to be in fairly good agreement with the experimental data reported in the

literature for laminar-to-turbulent transition (see, for example, Sleath 1984; Jensen *et al.* 1989; Lodahl *et al.* 1998), and also in very good agreement with the value $(Re)_{cr} = 1.58 \times 10^5$, obtained by a stability analysis (see Sleath 1984) as well as the asymptotic result $(Re)_{cr} = 1.5 \times 10^5$ of Tromans (1978) as $R/\delta_1 \rightarrow \infty$ (the plane boundary case) obtained from a stability analysis carried out for oscillatory flows in a circular pipe (R is the radius and δ_1 is the Stokes length). The results also agree well with the DNS simulations of Akhavan *et al.* (1991*b*), Vittori & Verzicco (1998) and Costamagna *et al.* (2003), as detailed in §4.2.3. At this juncture, we recognize the following comment made by one of the referees of this paper: 'When comparing experimental values for transitional and critical Reynolds number obtained through theoretical stability analysis (i.e. when linear disturbances start to grow), any correspondence in the values is usually just a coincidence', although the preceding comparison indicates that the correspondence between the experimentally obtained values and the theoretically obtained ones appears to be fairly good.

Secondly, figure 10 shows that, for a given value of Re, spots first emerge at a phase value in a broad interval of ωt. For example, for $1.5 \times 10^5 < Re < 2.5 \times 10^5$, spots would emerge at any phase between $\omega t = 103°$ and $153°$.

Thirdly, it is seen that the present data points, not surprisingly, fall into the transitional-regime area of Jensen *et al.* (1989), the area between the two thick, solid curves in the diagram. It is interesting to note that the flow-regime data of Jensen *et al.* (1989) were obtained through the flow-resistance information (attained by the bed shear stress measurements).

Fourthly, figure 10 further shows that the turbulent spots emerge earlier and earlier as the Reynolds number is increased. (For example, they emerge as early as at $\omega t = 56°$ when $Re = 8.5 \times 10^5$.) This is in agreement with the result of Jensen *et al.* (1989) that turbulence (characterized by the r.m.s. value of the fluctuations in the bed shear stress) first occurs just prior to the bed shear stress reversal (on average), and then spreads towards smaller and smaller values of phase with increasing Re. Jensen *et al.* (1989) note that turbulence first occurs just prior to the bed shear stress reversal because the adverse pressure gradient becomes relatively large and the velocity of near-bed fluid particles becomes relatively small at this phase value so that a very favourable environment forms for the initiation of turbulence. Note that the simulations performed by Blondeaux & Vittori (1994) show that, although for a somewhat smaller value of the Reynolds number ($Re = 0.8 \times 10^5$), the velocity field is characterized by large amplitude perturbations similar to those that would be induced by turbulent spots observed in this study. Of particular interest is Blondeaux & Vittori's (1994) simulations that show that transition to turbulence occurs at phase values similar to those corresponding to the inception of turbulent spots of this study.

The way in which the spots develop can be described with reference to figure 11 (test 2, half-cycle 10, $Re = 1.5 \times 10^5$). The spot first emerges in the form of two finite-length streaks (streaky white areas in figure 11*a*). Subsequently, the streaks develop twisting and turning motions (figure 11*b*, *c*), which are followed by the appearance of additional longitudinal streaks (figure 11*c*, *d*). The new streaks themselves develop twisting and turning motions and break into smaller structures, and the process continues, presumably resulting in the arrowhead-shaped turbulent spot similar to that described in conjunction with figure 9. This observation is analogous to that made for steady boundary layers (e.g. Gad-el-Hak, Blackwelder & Riley 1981; Perry, Lim & Teh 1981; Chambers & Thomas 1983; Browand & Plocher 1985; Seifert & Wygnanski 1995; Matsubara & Alfredsson 2001).
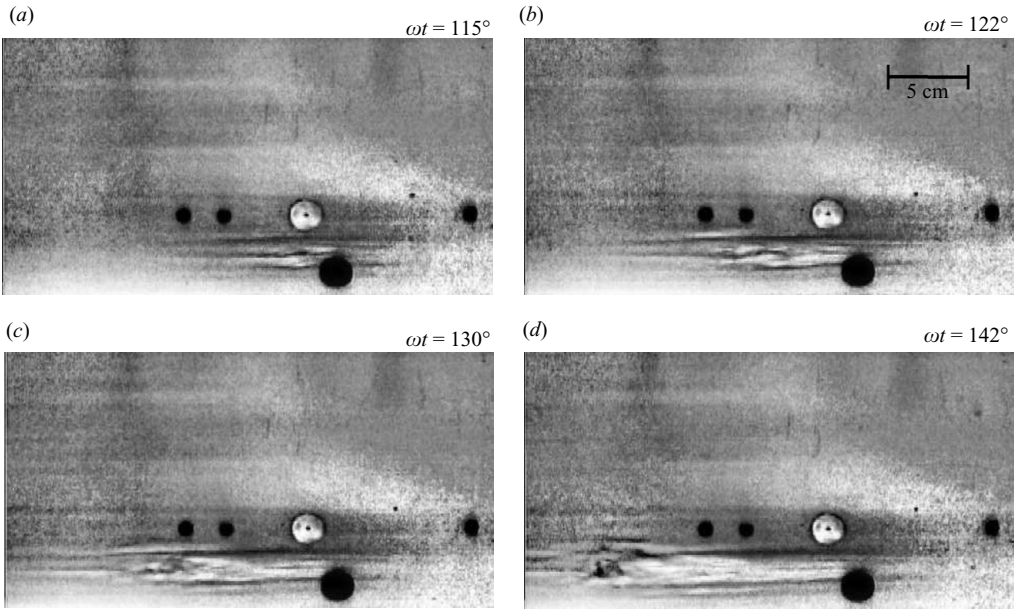
FIGURE 11. Inception of turbulent spot. $Re = 1.5 \times 10^5$. Flow direction from right to left.
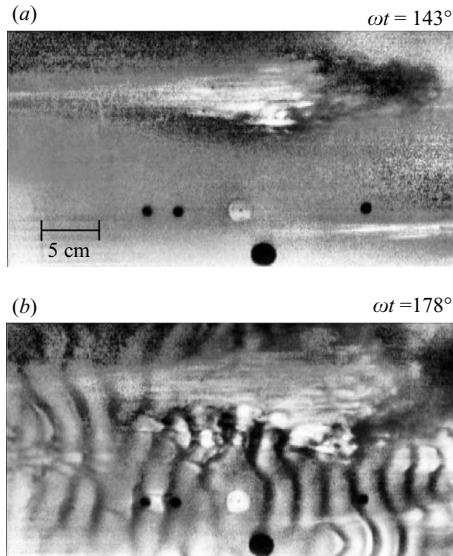

FIGURE 12. Turbulent spots and vortex tubes occur concurrently. Test 7, half-cycle 3. $Re = 3.0 \times 10^5$. Free-stream flow direction from left to right.

Turbulent spots can occur concurrently in space (see Carstensen 2006). As the flow develops during the half-cycle, turbulent spots grow in size (as described in conjunction with figure 9) and number, and eventually they merge to form the fully developed turbulent boundary layer (area marked turbulent in figure 10).

Turbulent spots can also occur simultaneously with vortex tubes; figure 12 (test 7, half-cycle 3, $Re = 3 \times 10^5$). In figure 12(*a*), it is seen that there is a turbulent spot

developing, but no vortex tubes have emerged yet at this phase, $\omega t = 143°$. However, by the time $\omega t = 178°$, vortex tubes have emerged and begin to develop (figure 12b). No vortex tubes are present inside the turbulent spot because the flow here is no longer in the laminar regime. Therefore, no quasi-two-dimensional inflection point instabilities develop inside the spot, and hence no vortex tubes emerge. In addition, the near-bed flow reversal outside the spot has already taken place at $\omega t = 135°$ while, inside the spot, this is delayed to $\omega t \approx 170°$ (see supplementary movie 4). The range of the Reynolds number in which vortex tubes and turbulent spots can exist concurrently is $1.5 \times 10^5 < Re < 3 \times 10^5$. The lower bound of the latter interval is the critical Re for the inception of turbulent spots (figure 10), and the upper bound is the largest Re beyond which no vortex tubes are observed (figure 6).

4.2.2. *Bed shear stress under turbulent spots*

Figure 13 displays a video sequence (test 6, half-cycle 4 with $Re = 4.5 \times 10^5$) illustrating two successive turbulent spots, which both pass over the hot-film probe (see supplementary movie 2). The first spot passes over the hot-film probe during the phase interval $91.5° < \omega t < 96°$ (figure 13a,b) and the second spot during the phase interval $140° < \omega t < 148°$ (figure 13c,d). The bed shear stress time series for this half-cycle (and thus the response of the bed shear stress to the passages of the two successive turbulent spots over the hot film) is shown in figure 14. The figure shows that the first spike in the bed shear stress (A) coincides with the passage of the first turbulent spot (spot A in figure 13a,b), and the second spike (B) coincides with the passage of the second turbulent spot (spot B in figure 13c,d). Similar spikes in near-bed velocity and wall shear stress signals have been observed by previous researchers in conjunction with laminar-to-turbulent transition in oscillatory boundary layers; Hino *et al.* (1976) in near-wall velocity signals and Jensen *et al.* (1989) and Lodahl *et al.* (1998) in wall shear stress signals. However, this study, for the first time, relates the previously observed spikes in the wall shear stress signal (and in the near-bed velocity signal) to turbulent spots.

There is a considerable difference in the shape of the two spikes in figure 14, spikes A and B. The bed shear stress data collected in the experiments show that there is a large variation in shape as well as in phase of the spikes. Figure 15 shows additional time-series of the bed shear stress. (We note that no turbulent spots were captured occurring just over the hot film in the range $1.5 \times 10^5 < Re < 1.9 \times 10^5$, although they occurred elsewhere as revealed by the flow visualization.) The large variation in the shape and phase of occurrence of the spikes is linked to factors such as the size and phase of spots; whether or not they are merged; and also equally important, their position relative to the hot-film probe.

The turbulence associated with the turbulent spot brings momentum-rich fluid from the outer flow to the near-bed area. Therefore, the higher the momentum of the outer-flow, the larger the magnitude of the spike in the bed shear stress. The momentum of the outer flow is highest at $\omega t = 90°$, and therefore the spikes should be largest around this phase value (e.g. figure 14, and for the single spikes in figure 15c–f). Figures 14 and 15 show that the magnitude of a spike in the bed shear stress signal can be as much as a factor of 3 or 4 larger (sometimes even larger) than the maximum bed shear stress caused by the maximum free-stream flow velocity. Clearly, this has large implications for sediment transport both in the laboratory and in the field.

As regards the effect of the size of the spot, the larger the spot, the longer the time during which it travels over the hot-film probe, and therefore large spots generate multiple spikes over a broad range of the phases. However, the spatial position of the turbulent spot relative to the probe is also important, as already pointed out. If
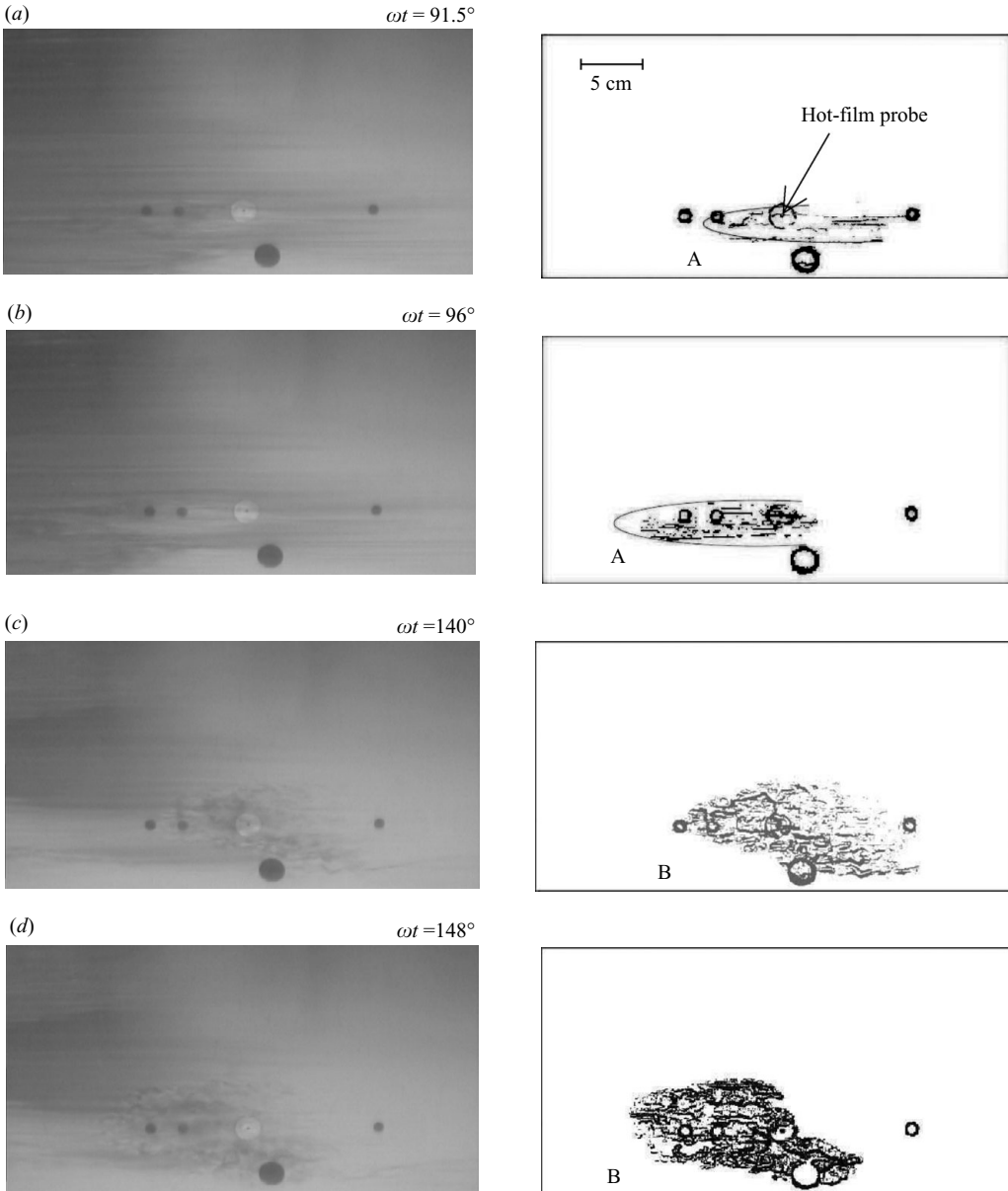
FIGURE 13. Video sequence (plan view) illustrating two successive turbulent spots which both pass over the hot-film probe; see also supplementary movie 2. Test 6, half-cycle 4. $Re = 4.5 \times 10^5$. Free-stream flow direction from right to left.

only a small portion of the spot is passing over the probe, this will appear in the bed shear stress trace as a relatively narrow spike or vice versa. Thus, the width of the spike is not a direct measure of the size of the turbulent spot.

Figure 16 shows further traces of bed shear stress for four more Reynolds numbers, from $Re = 1.2 \times 10^6$ to 5.0×10^6. (Note that the vertical scales in figure 16 are a factor of 2 larger than those in figure 15.) The Reynolds numbers in figure 16 were too high to track turbulent spots as identifiable, individual, coherent flow structures in
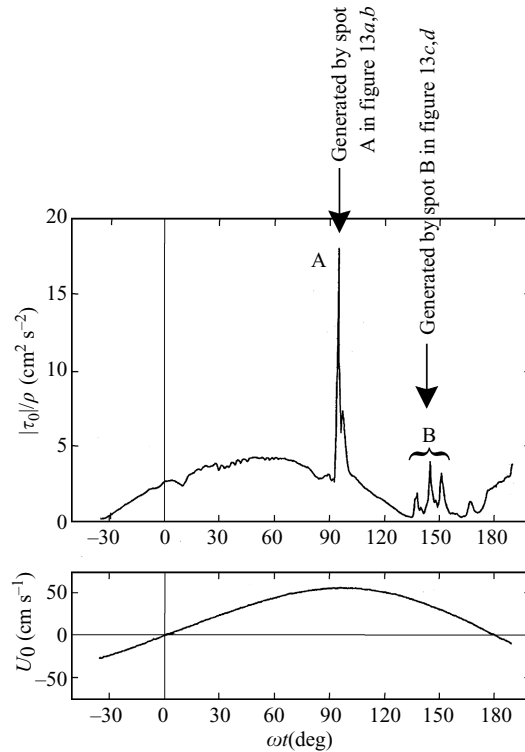
FIGURE 14. Traces of bed shear stress and free-stream velocity corresponding to the passage of the two turbulent spots over the hot-film probe illustrated in figure 13. $Re = 4.5 \times 10^5$.

flow visualization (the flow, for the most part, being in the fully developed turbulent regime where turbulent spots are merged, the area marked 'turbulent' in figure 10). Nevertheless, the bed shear stress was measured to obtain a complete picture of the process. Figure 16 clearly shows that turbulence is generated earlier and earlier in phase as Re is increased. With $Re = 5.0 \times 10^6$, turbulence is generated over the entire half-period, in agreement with our previous research (Jensen *et al.* 1989). Note that this conclusion is also in good agreement with the results of the DNS calculations of Vittori & Verzicco (1998) and Costamagna *et al.* (2003), namely that the turbulent velocity fluctuations increase in strength, and the decelerating part of the cycle during which they are observed becomes longer with increasing Re.

4.2.3. *Comparison with the results of others and discussion*

Hayashi & Ohashi (1982) reported what they called flow disturbances which '... appear on the bed and are deformed to U-shaped loops...' (see their figure 16c–f). They did not combine the visual and quantitative techniques that would have otherwise enabled them to relate the observed flow disturbances to flow quantities. The present authors believe that the flow disturbances in Hayashi & Ohashi's (1982) experiments were turbulent spots. No direct comparison could be made with Hayashi & Ohashi's results as they did not specifically give data with regard to the critical Reynolds number, the phase where the flow disturbances first appear and the way in which they develop. However, the following aspects are worth mentioning: Hayashi & Ohashi's still photographs illustrate that (*a*) their flow disturbances can exist concurrently (figure 16 of Hayashi & Ohashi 1982), and (*b*) they can also occur
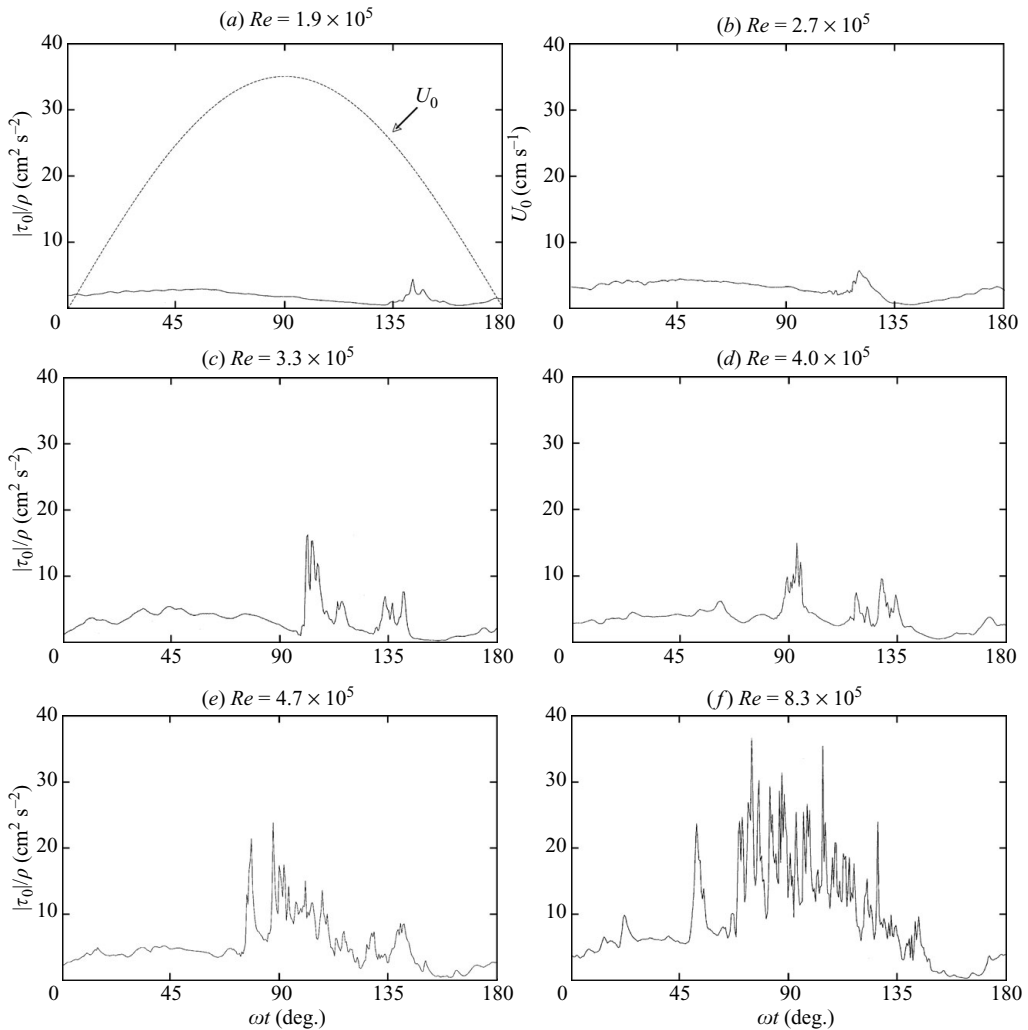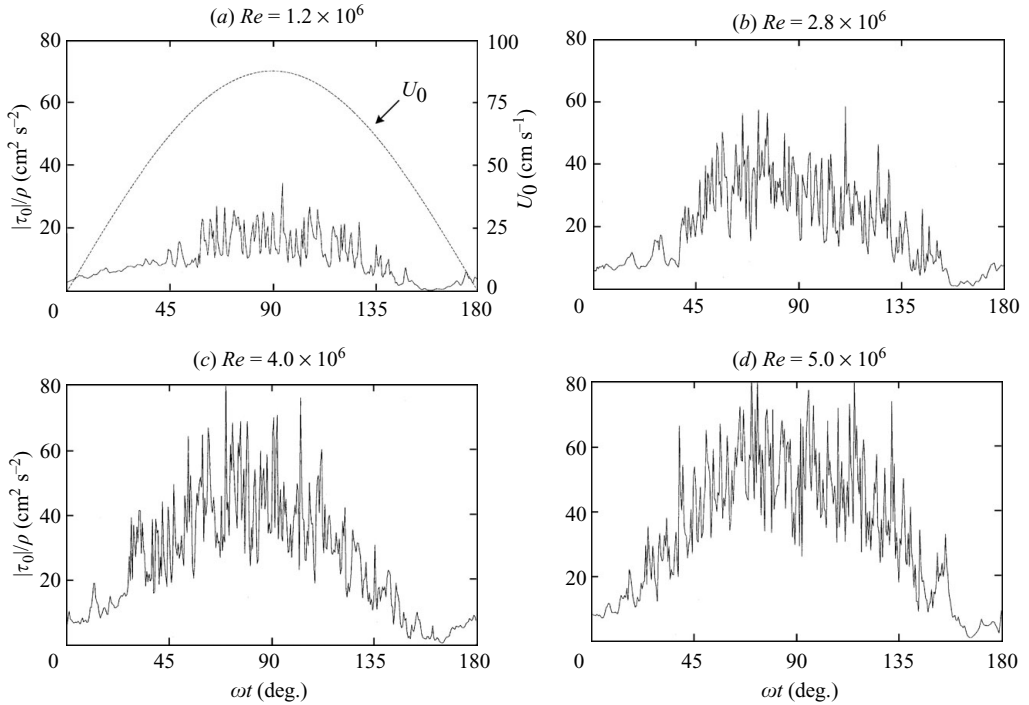
FIGURE 15. Traces of bed shear stress for different *Re* numbers in the transitional regime.

concurrently with vortex tubes (figures 16 and 17 of the same paper), in agreement with the present study.

As mentioned previously, Sarpkaya (1993) conducted an extensive series of flow visualization experiments. The objective was to examine the inception and response of low-speed streaks and other turbulence structures to periodic acceleration and deceleration of oscillatory flow to elucidate the mechanisms of transition to turbulence. On the basis of these experiments, Sarpkaya (1993) gave a very detailed description of the time development of longitudinal streaks, starting from their inception to their evolution and eventually to their destruction during the course of the flow. Although he did not specifically describe the observed streaks as part of a turbulent spot, there are striking similarities between the structures observed by Sarpkaya (1993; see e.g. the sequence in figure 7 of his paper) and those observed in this study. One difference, however, is that Sarpkaya (1993) reports that '... a series of events regarding longitudinal streaks was observed when *Re* was increased to

FIGURE 16. Traces of bed shear stress for large *Re* numbers.

$Re \approx 9 \times 10^4$–$1.1 \times 10^5 \ldots$', corresponding to the critical Reynolds number where turbulent spots first emerge in the context of the present study. (The presence of longitudinal streaks was actually observed even earlier in the study of Sarpkaya, when *Re* was set at $Re \approx 8 \times 10^4$; however, Sarpkaya notes that '... these streaks remained perfectly straight, smooth, and moved small amounts toward and away from each other with no visible interaction, and subsequently disappeared during the acceleration period...'.) The 'critical' Reynolds number at which the streaks first develop into what we interpret a turbulent spot in Sarpkaya's study, $Re \approx 9 \times 10^4$–1.1×10^5, is somewhat smaller than the critical Reynolds number of the present study, $Re = 1.5 \times 10^5$. The exact value of the critical Reynolds number may vary from study to study, however, depending on the disturbance level in different facilities. Sarpkaya (1993, p. 108) also remarks on this. As an example, our previous research (Fredsøe *et al.* 2003) clearly demonstrated that the transition to turbulence occurred earlier, at a much lower Reynolds number (like $Re \approx (5–6) \times 10^4$) when a field of external turbulence was introduced into the flow.

Vittori & Verzicco's (1998) DNS simulation results showed that the transition from what they call the disturbed laminar regime to the intermittent turbulent regime takes place at $(Re)_{cr} = 1.5 \times 10^5$, which is in very good agreement with the present experiments. This result was later confirmed by Costamagna *et al.*'s (2003) DNS simulations, wherein they investigated coherent structures, using the data obtained from simulations. For the intermittently turbulent-regime flows, their flow visualization in the numerical tests clearly showed the presence of low-speed streaks (Costamagne *et al.* 2003; figures 12 and 13, where $Re = 3.2 \times 10^5$), which resemble quite well the streaks inside the turbulent spots observed in the present experiments

(e.g. figure 9). We also note that their flow visualization also illustrates the formation and time development of low-speed wall streaks (the sequence of flow visualization frames in figures 15 and 16 of Costamagna *et al.* 2003). A whole turbulent spot was not simulated, however, by Costamagna *et al.* simply because the goal of the study was to isolate the basic flow unit and to study its 'morphology' and dynamics. Therefore, they aimed to keep the size of the computational box as small as possible to reproduce the process of turbulence generation (following Jimenez & Moin 1991). (In this connection, we note the following. Costamagna *et al.* report that a run has been made doubling the size of the computational box in both the streamwise and spanwise directions with dimensions 1290 and 640 in wall units, respectively. It turns out that even this size is small compared with the size of the turbulent spots shown in the sequence of video frames in figure 9.)

Akhavan *et al.* (1991*b*) carried out a hydrodynamic instability analysis for an oscillatory flow between two parallel plates. They investigated the flow instability for a variety of disturbances, tracking the time evolution of the disturbance by the DNS of the Navier–Stokes equations. Three kinds of disturbances were investigated: (*a*) infinitesimal disturbances, (*b*) finite-amplitude two-dimensional disturbances and (*c*) infinitesimal three-dimensional disturbances superimposed on finite-amplitude two-dimensional ones. The first kind of disturbances, although associated with a least-stable wavenumber, were shown to experience a monotonic decay with time, and therefore cannot be responsible for the transition. (We shall return to this point shortly.) Similarly, the second kind of disturbances also did not result in instability. However, Akhavan *et al.*'s simulations showed that the two-dimensional finite-amplitude disturbances are susceptible to growth in the presence of three-dimensional disturbances, and hence transition to turbulence could be explained by a so-called secondary instability mechanism, i.e. a mechanism in which two-dimensional finite-amplitude waves are unstable to three-dimensional infinitesimal disturbances. Such an instability mechanism has been investigated by Orszag & Patera (1983) for a wide variety of wall-bounded parallel shear flows, including plane Poiseuille flow, plane Couette flow, flat-plate boundary layers and pipe Poiseuille flow. With this kind of mechanism, Akhavan *et al.* (1991*b*) were able to predict well the critical value of the Reynolds number, $(Re_\delta)_{cr} \sim 500$ (or alternatively $(Re)_{cr} \sim 1.25 \times 10^5$), and the statistics of the resulting turbulent flow. Of particular interest is the resemblance of a predicted second peak in the phase-resolved turbulence energy during the half-cycle of the motion (figure 16 of Akhavan *et al.* 1991*b*) and that of the present bed shear stress measurements for the transitional Reynolds numbers (figures 14 and 15*c–e*).

At this juncture, it is interesting to discuss the role of the observed vortex tubes in the initiation of turbulence. Clearly, the observation of vortex tubes is not new, and this kind of instability is well understood. However, this study has shown experimentally for the first time that the inception of turbulence is not linked to the instability that generates vortex tubes. This is on the following grounds: (*a*) The vortex tubes have finite lifespans, as indicated in §4.1.1, and therefore cannot be sustained; (*b*) The present bed shear stress measurements show that, for the same Reynolds number, the high-frequency oscillations in the bed shear stress signal generated by these two-dimensional, 'regular' flow structures are one order of magnitude smaller than the turbulence generated by turbulent spots (§4.1.2); and (*c*) The present experiments offer no evidence towards any linkage between the generation of turbulent spots and the vortex tubes. In this context, we note that the spectral solution of the Orr–Sommerfeld equation of Akhavan *et al.* (1991*b*) (mentioned in the preceding paragraphs) indicated a least stable wave with $\lambda/\delta = 5.33$ (corresponding to the inflectional point instability,

the mechanism behind the present vortex tubes, with an estimate of the critical Reynolds number of $(Re_\delta)_{cr} \sim 85$). Akhavan *et al.*'s simulations of the time evolution of infinitesimal disturbances with the aforementioned least-stable wavelength showed that the disturbances, after an initial growth, experienced a monotonic decay, and therefore could not be sustained, and cannot explain the transition to turbulence in oscillatory boundary layers, in agreement with the present observations.

As regards the turbulent spots, the present observations have revealed for the first time that the inception of turbulence is associated with the generation of turbulent spots, an important feature not disclosed for oscillatory boundary-layer flows by the previously discussed experimental and theoretical investigations. The present experimental setup enabled us to visualize the whole spot, from its generation to its destruction throughout its evolution in phase space. It also enabled us to visualize the occurrence of more than one turbulent spots concurrently in physical space, as well as to visualize the simultaneous occurrence of turbulence spots and vortex tubes. Furthermore, the present observations revealed that the critical Reynolds number for the appearance of turbulence spots coincides with that found for the onset of three-dimensional turbulence observed in the experimental and theoretical studies. Also, the synchronized bed shear stress measurements and the flow visualization revealed the 'signature' of the individual spots on the bed shear stress signal as spikes in the decelerating phase of the motion, therefore settling the long-debated issue regarding the origin of the observed spikes. We believe that all this information is new and sheds further light onto the process of laminar-to-turbulent transition in oscillatory boundary layers.

Finally, we discuss a remark made by one of the referees, namely 'From the studies of, for example, Vittori & Verzicco (1998) and Costamagna *et al.* (2003), the role of extremely small wall imperfections have a large influence on the transition process. One is therefore left wondering about the role of the hot-film sensor and the dummy probes apparent on the flow visualization video frames. Could it be that the spots appear at not-so-random locations because of the presence of these probes.' As emphasized earlier, both the hot-film sensor and the dummy probes were mounted flush to the bottom of the tunnel and special care was taken to ensure that absolutely no disturbance was introduced to the flow by these probes. Nevertheless, as a further check, the video frames were checked carefully if there was any evidence of the initiation of the turbulent spots on or near these probes. No such evidence was found (see also the video frames presented in figures 9 and 11–13). Additionally, a quantitative analysis has been carried out to see if the spanwise position of the turbulent spots is correlated with the locations of these probes. Figure 17 presents the frequency histograms of the spanwise position of the turbulent spots. The data are grouped according to the *Re* number. The locations of the probes are also marked in the figure. This figure shows that there is no correlation between the spanwise position of the turbulent spots and the locations of the probes, and this is irrespective of *Re*, revealing that the turbulent spots appeared at random locations.

5. Coherent structures in combined oscillatory flow and current

5.1. *Vortex tubes*

The inflection point instability (and therefore the inception of vortex tubes) is governed by the Reynolds number, *Re*, in the case of pure oscillatory flow. In the case of combined oscillatory flow and current, there is one additional parameter, Re_c, the Reynolds number corresponding to the current component of the combined flow; see (7) and (8). This latter Reynolds number reduces to the usual definition $Re_c = (VD)/\nu$ in the case of a circular pipe where $R_h = D/4$ (*D*, the pipe diameter).
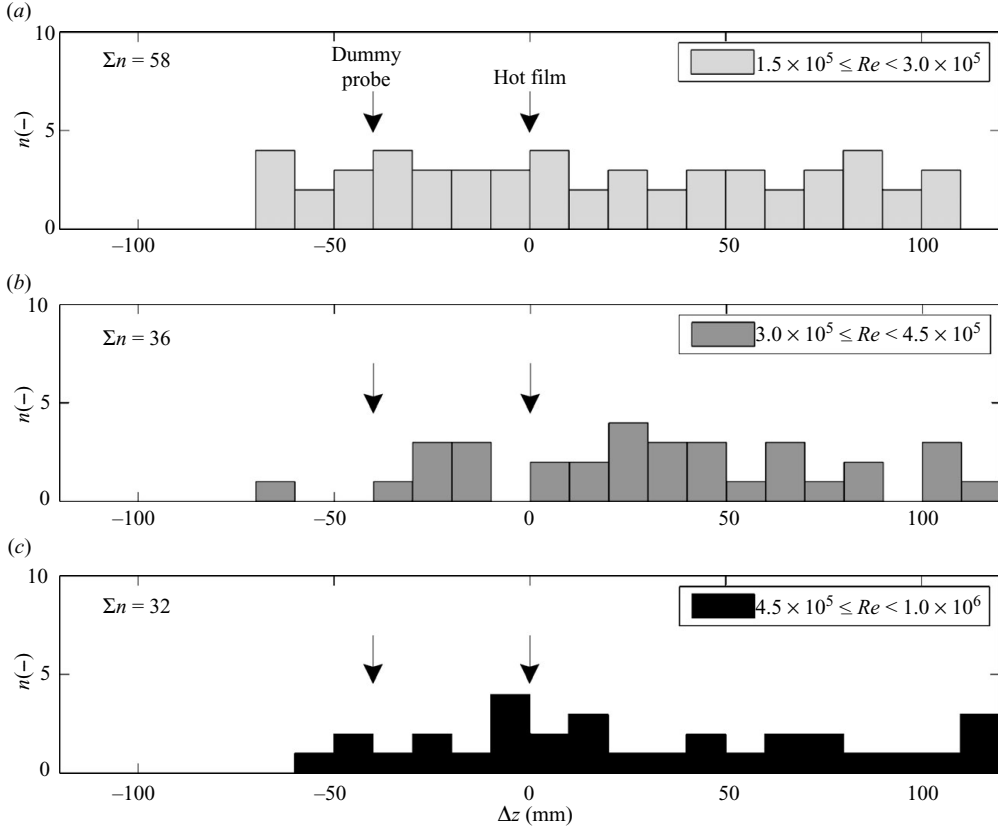
FIGURE 17. Frequency histograms of the spanwise position of the turbulent spots. Sample sizes are 58 (*a*), 36 (*b*) and 32 (*c*).

There is a third parameter, namely R_h/δ_1, the quantity R_h is the hydraulic radius defined in (8), and δ_1 is the Stokes length given in (10), as pointed out in our previous study (Lodahl *et al.* 1998); however, this parameter loses its significance for large R_h/δ_1 (Lodahl *et al.* 1998). This parameter in the present experiments was $R_h/\delta_1 = 8.3\,\mathrm{cm}/0.17\,\mathrm{cm} = 47$. Although not in the context of the inception of vortex tubes, the instability data (experimental and theoretical) regarding the transition to turbulence collected by Lodahl *et al.* (1998, figure 3), including Troman's (1978) theoretical and experimental data and Lodahl *et al.*'s own experimental data, for oscillatory flow in a circular pipe, suggest that results converge when $R_h/\delta_1 > 5$. Tuzi & Blondeaux's (2008) recent numerical simulations confirm the preceding finding where the latter authors recovered the plane-wall case when $R_h/\delta_1 > 4.5$.

Another important non-dimensional parameter is the ratio of the current velocity to the oscillatory flow velocity, V/U_{0m}, in which V is the cross-sectional average velocity corresponding to the current component of the combined flow; (6). This quantity can be worked out in terms of the other three non-dimensional parameters Re, Re_c and R_h/δ_1 as follows:

$$\frac{V}{U_{0m}} = \frac{1}{4\sqrt{2}(R_h/\delta_1)} \frac{Re_c}{Re^{1/2}}. \tag{15}$$

Any set of three independent non-dimensional parameters can be selected among Re, Re_c, R_h/δ_1 and V/U_{0m}, to describe the flow in the case of the combined oscillatory
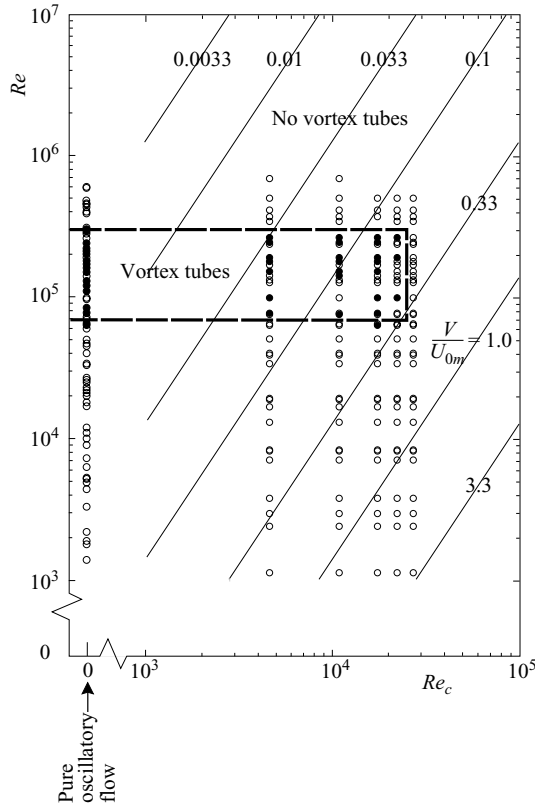
FIGURE 18. Vortex tube data in the case of the combined oscillatory flow and current. Empty circles mean no vortex tubes. Filled circles denote vortex tubes. (R_h/δ_1 value is maintained constant at $R_h/\delta_1 = 47$.)

flow and current. We choose Re, Re_c and R_h/δ_1, following Lodahl *et al.* (1998). Nevertheless, similar to our previous work (Lodahl *et al.* 1998), the lines representing the values of V/U_{0m}, calculated from (15), are indicated in figures 18 and 19, to emphasize the magnitude of the current relative to the oscillatory flow.

Figure 18 displays the vortex tube data. All the data points associated with vortex tubes (filled circles) correspond to the half-cycle in which the oscillatory flow and the current are in the same direction. This is with the exception of two instances where vortex tubes were observed for the half-cycle in which the oscillatory flow and the current were in the opposite direction. This may be attributed to the fact that the slope of the velocity profile at the inflection point, du/dy, is not large enough in this half-cycle to cause instability, i.e. to generate vortex tubes as many as in the half-cycle where the oscillatory flow and the current are in the same direction. To the authors' knowledge, no hydrodynamic instability theory is yet available, investigating the instability caused by the inflection point in the case of combined oscillatory flow and current, to shed light onto the observed difference in the instability between the two half-cycles.

Now, the dashed line in figure 18 divides the (Re, Re_c) plane into two parts: the area where vortex tubes are observed and that where no vortex tubes are observed. Firstly, it is seen from the figure that vortex tubes are not generated for the current Reynolds number above $Re_c = 2.2 \times 10^4$. This is because, for such large Reynolds
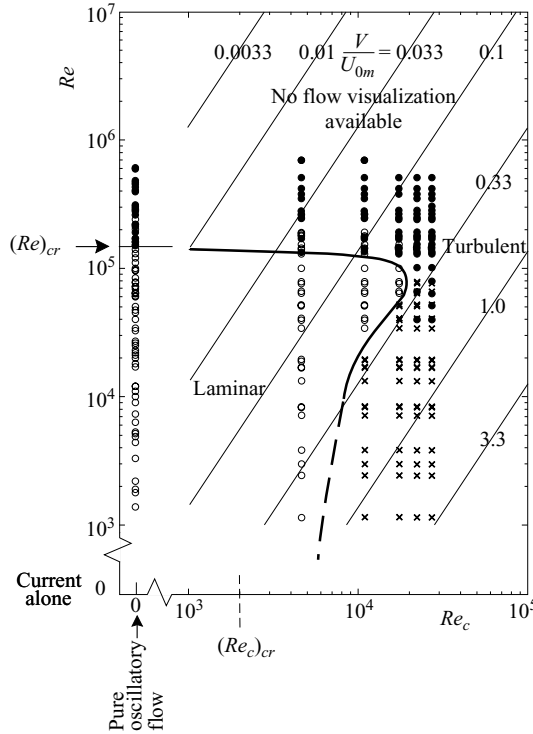
FIGURE 19. Turbulent spot data in the case of the combined oscillatory flow and current. Empty circles, laminar; filled circles, turbulent spot; crosses, current turbulence.

numbers, the flow is in the turbulent regime, as will be seen later, and therefore no inflectional-point shear layer instability will be generated, and hence there will be no inception of any vortex tubes. Secondly, the Reynolds number range where vortex tubes are observed in the case of the pure oscillatory flow, $7 \times 10^4 < Re < 3 \times 10^5$, is apparently uninfluenced by the presence of current. This is simply because the flow in the 'vortex tubes' area is in the wave-dominated regime ($V/U_m < O(0.2–0.3)$), as seen from figure 18, and hence an influence of current on the vortex tube generation is, in fact, unexpected.

The phase data (similar to figure 6) for the combined oscillatory flow and current tests, not shown here for reasons of space, indicated that all the data fall into scatter band of the pure oscillatory flow data displayed in figure 6. This is not unexpected because the vortex tubes appear to exist only in the wave-dominated flow regime and, therefore, the phase of their emergence and disappearance should be uninfluenced by the presence of the current in this regime. (The combined flow data can be seen in Carstensen 2006.)

Finally, similar to the case of the pure oscillatory flow, it is observed that the spacing between adjacent vortices, the wavelength, remains practically constant throughout their lifespan. Moreover, no correlation is found between the normalized wavelength λ/δ and the Reynolds numbers Re and Re_c in which δ is the boundary-layer thickness corresponding to the oscillatory component of the combined flow. From the data, the mean value of the wavelength is found to be

$$\frac{\lambda}{\delta} = 5.9 \qquad (16)$$

with $\sigma/\delta = 0.37$, where σ is the standard deviation calculated from the sample size $N = 26$. Again, this is also not unexpected because the vortex tubes appear to exist only in the wave-dominated flow regime.

5.2. *Turbulent spots*

Turbulent spots in an otherwise laminar boundary layer, as described for the case of pure oscillatory flow, were also identified in the case of combined oscillatory flow and current. Figure 19 displays the turbulent spot data (filled circles) plotted on the (Re, Re_c) plane where the velocity ratio, V/U_{0m}, contour lines also are plotted. The open-circles in the figure indicate the laminar regime combined flow, while the crosses indicate the combined flow with current-generated turbulence. The solid curve separates two areas on the (Re, Re_c) plane: laminar and turbulent. The difference between the turbulent spots and the current-generated turbulence is referred to in figure 20. This sequence indicates the following: (*a*) For the current alone case, the streaky pattern of the near-wall turbulent boundary-layer flow reported by many researchers, such as Kline *et al.* (1967) and Grass (1971) (see Cantwell 1981 for a review), is readily visible in the entire visualized area, also revealed by the present bed shear stress measurements. (*b*) As V/U_{0m} is decreased (small oscillatory component superimposed on the current), laminar-like patches start to appear in the otherwise turbulent boundary layer; and with further decrease of V/U_{0m} (larger oscillatory component superimposed on the current), the part of the half-period of the combined flow where there is a favourable pressure gradient is completely laminarized, while turbulent spots in an otherwise laminar boundary layer, as described for the pure oscillatory flow, form late in the part of the half-period where there is an adverse pressure gradient. (*c*) For small values of V/U_{0m}, such as $V/U_{0m} = O(0.1)$, the turbulent spots and the spike in the bed shear stress resemble those found for the case of the pure oscillatory flow (figure 14).

Now returning to figure 19, the following observations are made. Firstly, the data in figure 19 indicate that (*a*) the critical value of the Reynolds number, Re_c, will approach $(Re_c)_{cr} \approx 2 \times 10^3$ (the value known from steady flow research; Schlichting 1979, p. 451), as $Re \rightarrow 0$ (the current-alone case); and (*b*) the critical value of Re approaches $(Re)_{cr} = 1.5 \times 10^5$ (§4.2.1), as $Re_c \rightarrow 0$ (the oscillatory-flow-alone case).

Secondly, the transition to turbulence is delayed by superimposing an oscillatory flow on the current; for example, for $Re = 8 \times 10^4$, the transition to turbulence is delayed up to $(Re_c)_{cr} \approx 2 \times 10^4$, a value an order of magnitude larger than the critical value for the current-alone case, $(Re_c)_{cr} \approx 2 \times 10^3$.

Thirdly, the figure indicates that a turbulent current flow can be laminarized by introducing an oscillatory flow. It shows that the oscillatory flow Reynolds number range, Re, where the flow is laminarized varies with the current Reynolds number, Re_c. (This process, termed as re-laminarization, has been recognized by earlier researchers, such as Gilbrech & Combs 1963, Sarpkaya 1966, Ramaprian & Tu 1980 and Lodahl *et al.* 1998.)

Fourthly, it seems that turbulent spots may emerge at Re numbers smaller than 1.5×10^5, the critical value for the pure oscillatory flow for transition to turbulence; turbulent spots are observed at Re numbers as small as 3.5×10^4. (The latter occurs at the current Reynolds numbers $Re_c = 2–3 \times 10^4$.) The fact that transition may occur at much lower Reynolds numbers with current may be linked to a high free-stream turbulence level in this case, in agreement with our previous research (Fredsøe *et al.* 2003) on the influence of external field of turbulence on transition.
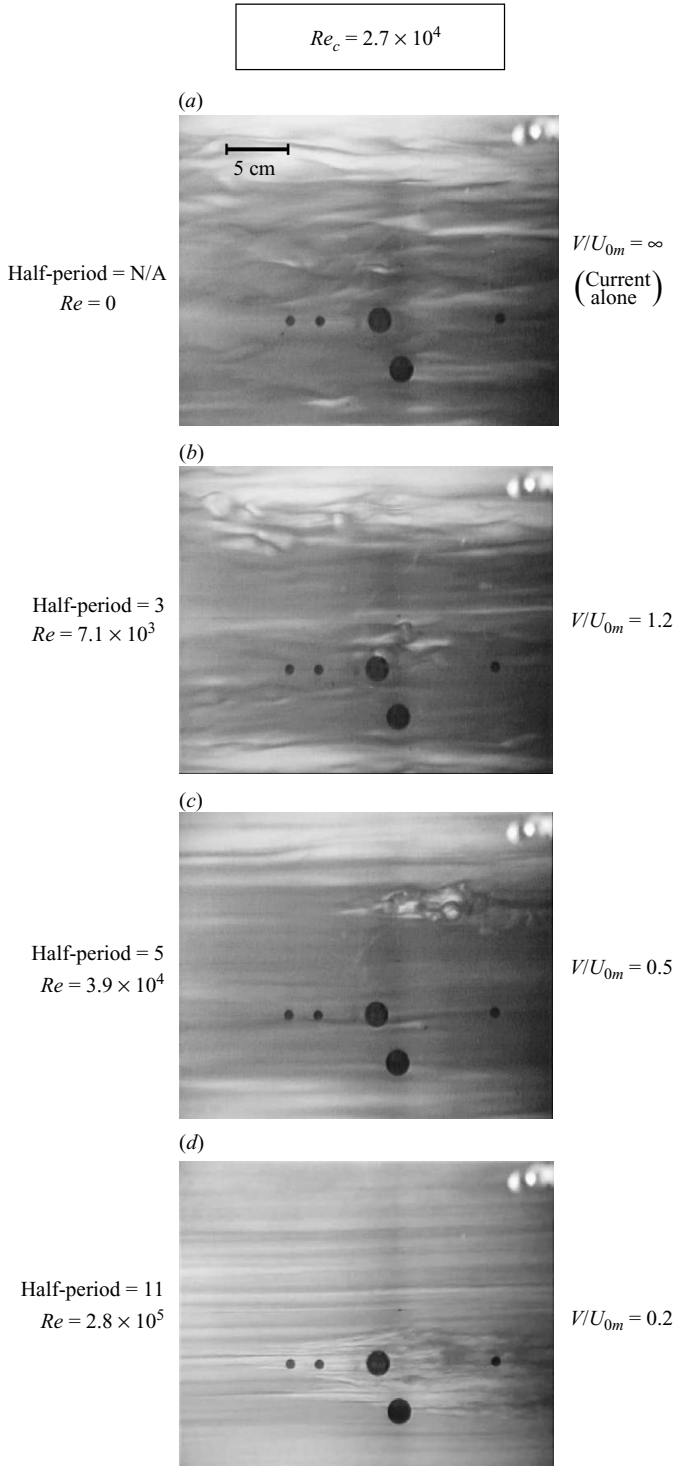
$$Re_c = 2.7 \times 10^4$$

(*a*)

Half-period = N/A
$Re = 0$

$V/U_{0m} = \infty$

$\left(\begin{matrix}\text{Current}\\\text{alone}\end{matrix}\right)$

5 cm

(*b*)

Half-period = 3
$Re = 7.1 \times 10^3$

$V/U_{0m} = 1.2$

(*c*)

Half-period = 5
$Re = 3.9 \times 10^4$

$V/U_{0m} = 0.5$

(*d*)

Half-period = 11
$Re = 2.8 \times 10^5$

$V/U_{0m} = 0.2$

FIGURE 20. Video frames illustrating the near-bed flow in the case of current alone (*a*) and in the case of combined flow with an increasing oscillatory flow velocity (*b*–*d*). Note the streamwise vortices visible with the elongated white areas in (*a*) and the arrowhead-shaped turbulent spots in (*c*) and (*d*).

The above observations are in complete agreement with our previous study (Lodahl *et al.* 1998), in which the wall shear stress in combined oscillatory flow and current was measured in three kinds of circular pipes with diameters of 19 cm, 9 cm and 1.1 cm. Lodahl *et al.* identified the flow regime, laminar or turbulent, from the time series of the wall shear stress, and using this information, constructed the neutral curve on the (Re, Re_c) plane. The neutral curve obtained from the present flow visualization observations (figure 19) is in good, qualitative agreement with those given in Lodahl *et al.* (1998). No direct comparison is made because of the differences in the flow environments of the two studies, the rectangular-section tunnel in the present study and the circular pipes in Lodahl *et al.*'s study.

6. Conclusions

(*a*) These observations show that two coherent flow structures exist in an oscillatory boundary layer for the transitional flow regimes: vortex tubes and turbulent spots.

(*b*) The vortex tubes are essentially two-dimensional vortices close to the bed extending across the width of the boundary-layer flow. These features emerge when the Reynolds number is in the range of $7 \times 10^4 < Re < 3 \times 10^5$.

(*c*) The imprint of these vortices in the bed shear stress is a series of small, insignificant kinks and dips.

(*d*) The turbulent spots are isolated areas close to the bed in an otherwise laminar boundary layer where the flow 'bursts' with violent oscillations. These features emerge when $(Re)_{cr} = 1.5 \times 10^5$. The emergence of the turbulent spots marks the onset of turbulence.

(*e*) Turbulent spots cause single or multiple spikes in the bed shear stress signal. The magnitude of these spikes can be as much as a factor of 3 or 4 larger (sometimes even larger) than the maximum bed shear stress associated with the maximum free-stream flow velocity. This has a significant implication for sediment transport, both in the laboratory and in the field.

(*f*) Similar coherent flow structures also exist in the case of the combined oscillatory flow and current.

(*g*) The Re range in which the vortex tubes emerge in the combined flow case is uninfluenced by the presence of the current. On the other hand, no vortex tubes are observed for the current Reynolds number, Re_c, larger than 2.2×10^4.

(*h*) Turbulent spots in the combined flow case are observed for Re numbers as small as $Re = 3.5 \times 10^4$.

Appendix. Flow resistance and phase

Figure 21 presents the flow resistance and phase data for the smooth-bed tests where the data of Jensen *et al.* (1989) also are plotted. No other data are plotted to keep the figure relatively simple. However, Jensen *et al.* (1989, figure 11) (and later Sarpkaya 1993, figures 4–6, including his own experimental data) made an extensive comparison of their flow resistance and phase data with the existing experimental and theoretical
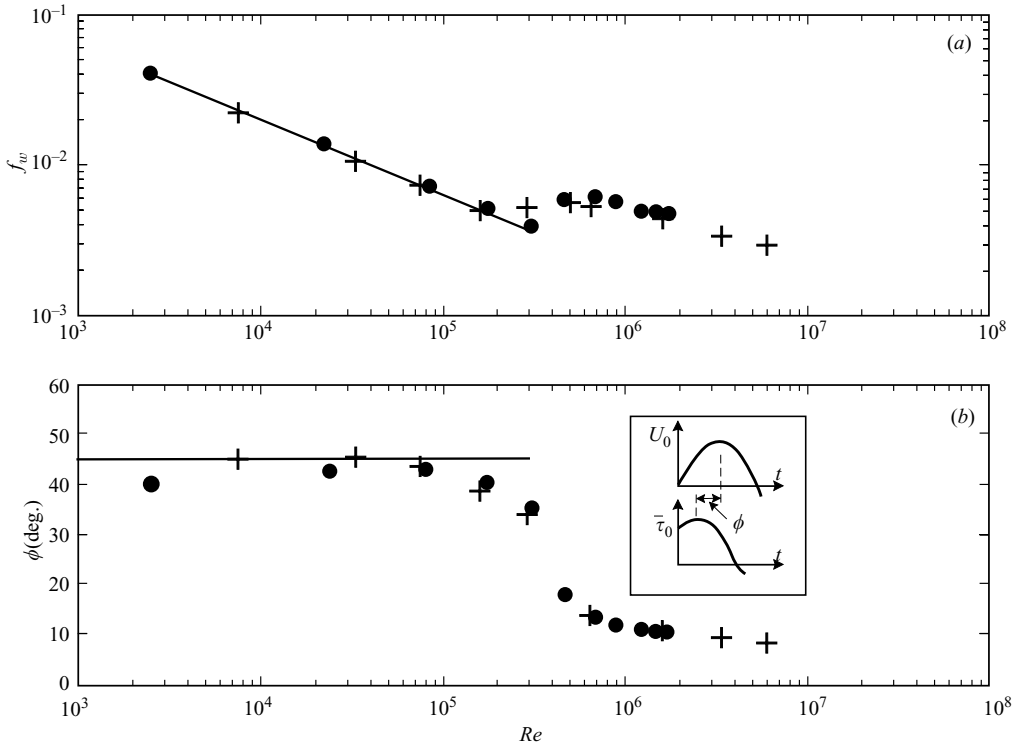
FIGURE 21. Wave friction coefficient and the phase lead of the bed shear stress for the present tests (circles) and Jensen *et al.* (1989) tests (crosses) where the oscillations were steady oscillations. Solid lines denote laminar solution.

work including Spalart & Baldwin's (1987) direct Navier–Stokes simulation, Fredsøe's (1984) theoretical solution, Kamphuis' (1975), Hino *et al.*'s (1983) and Sleath's (1987) experiments, and demonstrated that all the data are consistent with the exception that Spalart & Baldwin's numerical data and Kamphuis' experimental data deviate somewhat from the other data in the transitional *Re*-number range (Jensen *et al.* 1989, figure 11). In figure 21, f_w is the wave friction coefficient

$$f_w = \frac{2\tau_{0m}}{\rho U_{0m}^2}, \tag{A 1}$$

and ϕ is the phase lead of the bed shear stress over the free-stream velocity

$$\tau_0 = \tau_{0m} \; f(\omega t + \phi). \tag{A 2}$$

Figure 21 shows that the present data (where the amplitude of the motion is increased from rest steadily according to figure 3*a*) are in good agreement with those of Jensen *et al.* (1989), where the flow is driven with steady oscillations. However, some discrepancy is to be expected between the two cases for the turbulence quantities, $\overline{u'^2}$, $\overline{v'^2}$, ... and $\overline{\tau_0'^2}$, as the 'background' turbulence left from the previous cycles will not be the same in the two cases. Nevertheless, the organized structures (vortex tubes and turbulent spots), the focus of the present study, will be affected very little if not at all by the latter effect as these structures are associated with laminar-to-turbulent transition rather than fully developed turbulent flows.

Supplementary movies available at journals.cambridge.org/flm.

REFERENCES

AKHAVAN, R., KAMM, R. D. & SHAPIRO, A. H. 1991*a* An investigation of transition to turbulence in bounded oscillatory Stokes flows. Part 1. Experiments. *J. Fluid Mech.* **225**, 395–422.

AKHAVAN, R., KAMM, R. D. & SHAPIRO, A. H. 1991*b* An investigation of transition to turbulence in bounded oscillatory Stokes flows. Part 2. Numerical simulations. *J. Fluid Mech.* **225**, 423–444.

BATCHELOR, G. K. 1967 *An Introduction to Fluid Dynamics*. Cambridge University Press.

BERNALL, L. P. 1981 The coherent structures of turbulent mixing layers. PhD thesis, California Institute of Technology.

BLENNERHASSETT, P. J. & BASSOM, A. P. 2006 The linear stability of high-frequency oscillatory flow in a channel. *J. Fluid Mech.* **556**, 1–25.

BLONDEAUX, P. & SEMINARA, G. 1979 Transizione incipiente al fondo di un'onda di gravita. *Rendiconti Accad. Naz. Lincei* **67**, 407–417.

BLONDEAUX, P. & VITTORI, G. 1994 Wall imperfections as a triggering mechanism for Stokes-layer transition. *J. Fluid Mech.* **264**, 107–135.

BLONDEAUX, P. & VITTORI, G. 1999 Boundary layer and sediment dynamics under sea waves. In *Advances in Coastal and Ocean Engineering* (ed. P. L.-F. Liu), vol. 4, pp. 133–190. World Scientific.

BROWAND, F. 1966 An experimental investigation of instability of an incompressible, separated shear layer. *J. Fluid Mech.* **26**, 281–307.

BROWAND, F. & PLOCHER, D. A. 1985 Image processing for sediment transport. In *21st IAHR Congress*, pp. 19–23. Melbourne, Australia.

CANTWELL, B. J. 1981 Organized motion in turbulent flow. *Annu. Rev. Fluid Mech.* **13**, 457–515.

CARSTENSEN, S. 2006 Experimental investigation of coherent structures in wave boundary layers. PhD thesis. Technical University of Denmark, DTU Mekanik, Section of Coastal, Maritime and Structural Engineering.

CHAMBERS, F. & THOMAS, A. 1983 Turbulent spots, wave packets and growth. *Phys. Fluids* **26** (5), 1160–1162.

COSTAMAGNA, P., VITTORI, G. & BLONDEAUX, P. 2003 Coherent structures in oscillatory boundary layers. *J. Fluid Mech.* **474**, 1–33.

DAS, D. & ARAKERI, J. H. 1998 Transition to unsteady velocity profiles with reverse flow. *J. Fluid Mech.* **374**, 251–283.

DIXEN, M., HATIPOGLU, F., SUMER, B. M. & FREDSØE, J. 2008 Wave boundary layer over a stone-covered bed. *Coastal Engng* **55**, 1–20.

EMMONS, H. 1951 Laminar–turbulent transition in boundary layer. *J. Aeronaut. Sci.* **18** (7), 490–498.

FORNARELLI, F. & VITTORI, G. 2009 Oscillatory boundary layer close to a rough wall. *Eur. J. Mech.* B. *Fluids* **28**, 283–295.

FOSTER, D. L. 1997 Dynamics of the near shore wave bottom boundary layer. PhD thesis, Oregon State University.

FOSTER, D. L., HOLMAN, R. A. & BEACH, R. A. 1994 Sediment suspension events and shear instabilities in the bottom boundary layer. Coastal Dynamics 94. In *Proc. Intl Conf. on the Role of the Large Scale Experiments in Coastal Research, ASCE* (ed. A. S. Arcilla, M. F. Stive & N. C. Kraus), pp. 712–726. Universitat Politecnica de Catalunya, Barcelona, Spain.

FREDSØE, J. 1984 Turbulent boundary layer in wave-current motion. *J. Hydraul. Engng ASCE* **110**, 1103–1120.

FREDSØE, J., SUMER, B. M., KOZAKIEWICZ, A., CHUA, L. H. C. & DEIGAARD, R. 2003 Effect of externally generated turbulence on wave boundary layer. *Coastal Engng* **49**, 155–183.

FUHRMAN, D. R., FREDSØE, J. & SUMER, B. M. 2009*a* Bed slope effects on turbulent wave boundary layers: 1. Model validation and quantification of rough-turbulent results. *J. Geophys. Res.,* **114**, C03024, 1–16.

FUHRMAN, D. R., FREDSØE, J. & SUMER, B. M. 2009*b* Bed slope effects on turbulent wave boundary layers: 2. Comparison with skewness, asymmetry, and other effects. *J. Geophys. Res.*, **114**, C03025, 1–19.

GAD-EL-HAK, M., BLACKWELDER, R. & RILEY, J. 1981 On the growth of turbulent regions in laminar boundary layers. *J. Fluid Mech.* **110**, 73–95.

GILBRECH, D. A. & COMBS, G. D. 1963 Critical Reynolds numbers for incompressible pulsating flows in tubes. *Develop. Theor. Appl. Mech.* **1**, 292–304.

GRASS, A. J. 1971 Structural features of turbulent flow over smooth and rough boundaries. *J. Fluid Mech.* **50**, 223–256.

GRANT, W. D. & MADSEN, O. S. 1979 Combined wave and current interaction with a rough bottom. *J. Geophys. Res.* **84**, 1797–1808.

HANRATTY, T. J. & CAMPBELL, J. A. 1983 Measurement of wall shear stress. In *Fluid Mechanics Measurements* (ed. R. J. Goldstein), pp. 559–615. Hemisphere.

HAYASHI, T. & OHASHI, M. 1982 A dynamical and visual study on the oscillatory turbulent boundary layer. In *Turbulent Shear Flows 3*, pp. 18–33. Third International Symposium on Turbulent Shear Flows.

HINO, M., KASHIWAYANAGI, M., NAKAYAMA, A. & HARA, T. 1983 Experiments on turbulence statistics and structure of reciprocating oscillatory flow. *J. Fluid Mech.* **131**, 363–399.

HINO, M., SAWAMOTO, M. & TAKASU, S. 1976 Experiments on transition to turbulence in an oscillatory pipe flow. *J. Fluid Mech.* **75** (2), 193–207.

HO, C.-M. & HUERRE, P. 1984 Perturbed free shear layers. *Annu. Rev. Fluid Mech.* **16**, 365–424.

JENSEN, B. L., SUMER, B. M. & FREDSØE, J. 1989 Turbulent oscillatory boundary layers at high Reynolds numbers. *J. Fluid Mech.* **206**, 265–297.

JIMENEZ, J. & MOIN, P. 1991 The numerical flow unit in the near-wall turbulence. *J. Fluid Mech.* **225**, 213–240.

JUSTESEN, P. 1988 Turbulent wave boundary layers. Series paper 41, Institute of Hydrodynamic and Hydraulic Engineering, Technical University of Denmark.

KAMPHUIS J. W. 1975 Friction factor under oscillatory waves. *J. Waterway, Port, Coastal and Ocean Engineering* **101** (WW2), 135–144.

KEMP, P. H. & SIMONS, R. R. 1982 The interaction between waves and a turbulent current: waves propagating with the current. *J. Fluid Mech.* **116**, 227–250.

KEMP, P. H. & SIMONS, R. R. 1983 The interaction between waves and a turbulent current: waves propagating against the current. *J. Fluid Mech.* **130**, 73–89.

KLINE, S. J., REYNOLDS, W. C., SCHRAUB, F. A. & RUNSTADLER, P. W. 1967 The structure of turbulent boundary layers. *J. Fluid Mech.* **30**, 741–773.

LODAHL, C., SUMER, B. M. & FREDSØE, J. 1998 Turbulent combined oscillatory flow and current in a pipe. *J. Fluid Mech.* **373**, 313–348.

LOHMANN, I. P., FREDSØE, J., SUMER, B. M. & CHRISTENSEN, E. D. 2006 Large eddy simulation of the ventilated wave boundary layer. *J. Geophys. Res.* **111**, C06036, doi:10.1029/2005JC002946.

LUNDGREN, H. & JONSSON, I. G. 1961 Bed shear stress induced by a wave motion. Coastal Engineering Laboratory, Technical University of Denmark. Basic Research Progress Report, **1**, 3–5.

MATSUBARA, M. & ALFREDSSON, P. H. 2001 Disturbance growth in boundary layers subjected to free-stream turbulence. *J. Fluid Mech.* **430**, 149–168.

ORSZAG, S. A. & PATERA, A. T. 1983 Secondary instability of wall-bounded shear flows. *J. Fluid Mech.* **128**, 347–385.

PERRY, A., LIM, T. & TEH, E. 1981 A visual study of turbulent spots. *J. Fluid Mech.* **104**, 387–405.

RAMAPRIAN, B. R. & TU, S. W. 1980 An experimental study of oscillatory pipe flow at transitional Reynolds number. *J. Fluid Mech.* **100**, 513–544.

SALON, S., ARMENIO, V. & CRISE, A. 2007 A numerical investigation of the Stokes boundary layer in the turbulent regime. *J. Fluid Mech.* **570**, 253–296.

SARPKAYA, T. 1966 Experimental determination of the critical Reynolds number for pulsating Pouseuille flow. *Trans. ASME J. Basic Engng* **88**, 589–598.

SARPKAYA, T. 1993 Coherent structures in oscillatory boundary layers. *J. Fluid Mech.* **253**, 105–140.

SCHLICHTING, H. 1979 *Boundary Layer Theory*. McGraw-Hill.

SEIFERT, A. & WYGNANSKI, I. J. 1995 On turbulent spots in a laminar boundary layer subjected to a self-similar adverse pressure gradient. *J. Fluid Mech.* **296**, 185–209.

SLEATH, J. F. A. 1984 *Sea Bed Mechanics*. John Wiley & Sons.

SLEATH, J. F. A. 1987 Turbulent oscillatory flow over rough beds. *J. Fluid Mech.* **182**, 369–409.

SOULSBY, R. L., HAMM, L., KLOPMAN, G., MYRHAUG, D., SIMONS, R. R. & THOMAS, G. P. 1993 Wave-current interaction in the vertical. *Coastal Engng* **21**, 41–69.

SPALART, P. R. & BALDWIN, B. S. 1987 Direct simulation of a turbulent oscillating boundary layer. NASA Tech. Mem. 89460 Ames Research Center, Moffett Field, California.

SUMER, B. M. 2003 Experimental investigation of wave boundary layer. EUROMECH Colloquium No. 451, pp. 26–29. Taormina, Italy, General Lecture. PowerPoint presentation obtainable from the author (bms@mek.dtu.dk).

SUMER, B. M., JENSEN, B. L. & FREDSØE, J. 1987 Turbulence in oscillatory boundary layers. In *Advances in Turbulence* (ed. Gt. Comte-Bello & J. Mathieu), pp. 556–567. Springer.

TROMANS, P. S. 1978 Stability and transition of periodic pipe flows. PhD thesis, Cambridge University.

TUZI, R. & BLONDEAUX, P. 2008 Intermittent turbulence in a pulsating pipe flow. *J. Fluid Mech.* **599**, 51–79.

VITTORI, G. & VERZICCO, R. 1998 Direct simulation of transition in an oscillatory boundary layer. *J. Fluid Mech.* **371**, 207–232.